



**HAL**  
open science

# Solar chemical looping reforming of methane combined with isothermal H<sub>2</sub>O/CO<sub>2</sub> splitting using ceria oxygen carrier for syngas production

Srirat Chuayboon, Stéphane Abanades, Sylvain Rodat

## ► To cite this version:

Srirat Chuayboon, Stéphane Abanades, Sylvain Rodat. Solar chemical looping reforming of methane combined with isothermal H<sub>2</sub>O/CO<sub>2</sub> splitting using ceria oxygen carrier for syngas production. *Journal of Energy Chemistry*, 2020, 41, pp.60-72. 10.1016/j.jechem.2019.05.004 . hal-02163394

**HAL Id: hal-02163394**

**<https://hal.science/hal-02163394>**

Submitted on 10 Nov 2020

**HAL** is a multi-disciplinary open access archive for the deposit and dissemination of scientific research documents, whether they are published or not. The documents may come from teaching and research institutions in France or abroad, or from public or private research centers.

L'archive ouverte pluridisciplinaire **HAL**, est destinée au dépôt et à la diffusion de documents scientifiques de niveau recherche, publiés ou non, émanant des établissements d'enseignement et de recherche français ou étrangers, des laboratoires publics ou privés.

# Solar chemical looping reforming of methane combined with isothermal H<sub>2</sub>O/CO<sub>2</sub> splitting using ceria oxygen carrier for syngas production

Srirat Chuayboon<sup>a,b</sup>, Stéphane Abanades<sup>a,\*</sup>, Sylvain Rodat<sup>c,d</sup>

<sup>a</sup> Processes, Materials and Solar Energy Laboratory, PROMES-CNRS, 7 Rue du Four Solaire, 66120 Font-Romeu, France

<sup>b</sup> Department of Mechanical Engineering, King Mongkut's Institute of Technology Ladkrabang, Prince of Chumphon Campus, Chumphon 86160, Thailand

<sup>c</sup> Univ. Grenoble Alpes, INES, BP 332, 50 Avenue du Lac Léman, F-73375 Le-Bourget-du-lac, France,

<sup>d</sup> CEA-LITEN Laboratoire des Systèmes Solaires Haute Température (LSHT), F-38054 Grenoble, France

\*Corresponding author: Tel +33 (0)4 68 30 77 30

E-mail address: [stephane.abanades@promes.cnrs.fr](mailto:stephane.abanades@promes.cnrs.fr)

## Abstract

The chemical looping reforming of methane through the nonstoichiometric ceria redox cycle (CeO<sub>2</sub>/CeO<sub>2-δ</sub>) has been experimentally investigated in a directly irradiated solar reactor to convert both solar energy and methane to syngas in the temperature range 900-1050 °C. Experiments were carried out with different ceria shapes via two-step redox cycling composed of endothermic partial reduction of ceria with methane and complete exothermic re-oxidation of reduced ceria with H<sub>2</sub>O/CO<sub>2</sub> at the same operating temperature, thereby demonstrating the capability to operate the cycle isothermally. A parametric study considering different ceria macrostructure variants (ceria packed powder, ceria packed

powder mixed with inert  $\text{Al}_2\text{O}_3$  particles, and ceria reticulated porous foam) and operating parameters (methane flow-rate, reduction temperature, or sintering temperature) was conducted in order to unravel their impact on the bed-averaged oxygen non-stoichiometry ( $\delta$ ), syngas yield, methane conversion, and solar reactor performance. The ceria cycling stability was also experimentally investigated to demonstrate repeatable syngas production by alternating the flow between  $\text{CH}_4$  and  $\text{H}_2\text{O}$  (or  $\text{CO}_2$ ). A decrease in sintering temperature of the ceria foam was beneficial for increasing syngas selectivity, methane conversion, and reactor performance. Increasing both  $\text{CH}_4$  concentration and reduction temperature enhanced  $\delta$  with the maximum value up to 0.41 but concomitantly favored  $\text{CH}_4$  cracking reaction. The ceria reticulated porous foam showed better performance in terms of effective heat transfer, due to volumetric absorption of concentrated solar radiation and uniform heating with lower solar power consumption, thereby promoting the solar-to-fuel energy conversion efficiency that reached up to 5.60%. The energy upgrade factor achieved during cycle was up to 1.19. Stable patterns in the  $\delta$  and syngas yield for consecutive cycles with the ceria foam validated material performance stability.

**Keywords:** Chemical looping, Methane reforming, Ceria structure, Concentrated solar power, Syngas production,  $\text{H}_2\text{O}/\text{CO}_2$  splitting

## 1. Introduction

Concentrated solar power is a sustainable and desirable renewable-energy source for process heat to drive high-temperature thermochemical reactions, e.g. redox cycles. Of particular interest is solar energy conversion into transportable and dispatchable chemical fuels by water ( $\text{H}_2\text{O}$ ) or carbon dioxide ( $\text{CO}_2$ ) splitting using thermochemical redox cycles to

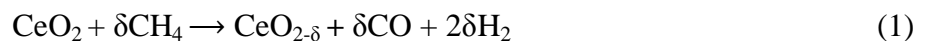
produce syngas (mixture of hydrogen ( $H_2$ ) and carbon monoxide ( $CO$ )). The resulting syngas can be further converted to liquid hydrocarbon fuel via Fischer-Tropsch [1] or utilized for production of methanol, ammonia, or dimethyl ether [2].

The conventional production of syngas through the conversion of methane ( $CH_4$ ) involves steam reforming [3], dry reforming with  $CO_2$  [4–7], and methane reforming over metal oxide redox materials [8–10] (partial oxidation of methane). The methane reforming over redox systems results in the partial oxidation of methane without the use of gaseous oxygen or catalysts and further allows operating the process as a cycle (because the solid oxide can be recycled back via oxidation with  $H_2O$  or  $CO_2$ ) while producing syngas. The heat required for such an endothermic reaction can be provided by solar energy using concentrating solar power technologies, thereby converting solar energy into transportable and storable chemical fuels [11–14]. This two-step combined process (methane reforming and  $H_2O/CO_2$  splitting) requires significantly lower reduction temperature as compared to the two-step oxide-based redox cycle [15,16] due to the aid of a reducing agent ( $CH_4$ ). Since the metal oxide reduction with  $CH_4$  and the  $H_2O/CO_2$  splitting steps usually proceed at similar temperatures, isothermal cycle operation is made possible, which reduces the constraints imposed by reactor materials as well as thermal radiation losses [17].

The feasibility of utilizing metal oxides (either non-volatile or volatile metals) as oxygen carriers for  $CH_4$  partial oxidation has been experimentally reported for ceria ( $CeO_2$ ) [9,18], cerium-based oxides [8,19,20], iron oxide [21], tungsten oxide [13], and zinc oxide [11,22]. Among them, the partial oxidation of  $CH_4$  with either doped or undoped ceria is particularly attractive owing to its capabilities for both rapid oxygen storage and release through lattice transfer, while retaining a stable crystallographic structure over a wide range of reduction extents [15], with reversible shift between  $Ce^{4+}$  and  $Ce^{3+}$  oxidation states [23,24].

Prior experimental study considering the partial oxidation of CH<sub>4</sub> using the redox properties of ceria was first reported by Otsuka et al. [9], without the utilization of solar energy. They demonstrated that the conversion of methane into syngas with a H<sub>2</sub>/CO ratio of 2 was possible, and the reduced ceria could be re-oxidized with CO<sub>2</sub> to produce CO. Then, both thermodynamic and experimental studies [25,26] with the combination of concentrated solar energy were considered. Krenzke and Davidson [25] studied the thermodynamics of the ceria cycle with methane. They indicated that coupling the reduction of ceria with the partial oxidation of methane enables isothermal cycling at 950 °C with high-quality syngas produced during the reduction step and maximum predicted solar-to-fuel efficiency of 40%. Welte et al. [14] experimentally investigated the methane reforming over ceria in a particle-transport reactor. This reactor achieved a bed-averaged oxygen non-stoichiometry ( $\delta$ ) as high as 0.25 at the expense of unreacted ceria particle being entrained by the produced syngas.

The chemical-looping methane reforming over ceria can be represented by two steps. First, the endothermic partial ceria reduction in the presence of CH<sub>4</sub> that reacts with lattice oxygen for the production of syngas with a H<sub>2</sub>/CO ratio of 2 suitable for methanol synthesis:



Second, the oxidation of partially-reduced ceria with H<sub>2</sub>O or CO<sub>2</sub>:



The advantages of the process combining partial oxidation of CH<sub>4</sub> and ceria redox cycle are: (i) the utilization of CH<sub>4</sub> in the reduction step allows for isothermal operation, thereby avoiding sensible heat losses taking place during temperature-swing cycle and eliminating the need for heat recovery, (ii) solid oxide is used in place of gaseous oxygen which eliminates the need for oxygen production from air, (iii) reduced ceria can be subsequently oxidized with either H<sub>2</sub>O or CO<sub>2</sub> in an oxidation step to produce additional syngas and complete the

cycle, (iv) deposited carbon on ceria structures can be concomitantly gasified and removed during the oxidation step, thus avoiding material deactivation and eliminating the requirement for expensive catalysts.

The ceria macrostructure plays a significant role on the performance of the combined two-step process in terms of conductive and radiative heat transfer across the material. Various metal oxide structures such as porous foams [15,16,26–29], textured plates [28], vertical pins [28], powder [30], powder mixed with inert material [23], multi-channeled honeycombs [31,32], felts [33] and three-dimensionally ordered macroporous (3DOM) ceramics [29, 34] have been studied for two-step thermochemical  $\text{H}_2\text{O}/\text{CO}_2$  splitting cycles in order to provide an effective interface for uniform concentrated solar energy absorption and sufficient surface area for supporting rapid chemical reactions. The powder bed structure or powder mixed with inert promoter [23] exhibited rapid oxidation rates; however at the expense of high radiative opacity, which may lead to undesired temperature gradients across the bed. Such a barrier can be tackled by using porous foam structures with high specific surface area [15-16], although heat transfer limitation may arise from their high optical thickness. Such reactive structures could therefore be applied advantageously to the solar-driven isothermal chemical looping reforming process with  $\text{CH}_4$  and oxidant gas ( $\text{H}_2\text{O}$  or  $\text{CO}_2$ ) alternately flowing through the oxide structure. Besides, different solar reactor concepts have been developed for thermochemical solar fuel production and applied to e.g. solar gasification or metal oxide redox cycles [35-41]. They can mainly be categorized as particle-based (encompassing packed or fluidized beds, entrained flows or particle clouds) or structured reactor technologies (volumetric porous receiver). However, versatile solar reactor operation applied to a large variety of ceria materials for methane reforming has not been considered to-date. The feasibility of isothermal solar-driven chemical looping methane reforming using ceria structures thus needs to be demonstrated in a flexible and scalable

solar-operated reactor able to achieve both process steps continuously with repeatable fuel production, reversible oxygen exchange and thermochemical performance stability.

Therefore, because of the noticeable advantages of the methane reforming over ceria and the beneficial effects of ceria structures, the present study aims to investigate the chemical looping process with different ceria oxygen carrier structures in a novel flexible solar reactor driven by real high-flux concentrated solar power, provided by a parabolic dish solar concentrator. The whole process was reliably operated and demonstrated for the first time in this work under real solar irradiation conditions. The effect of different ceria structures (ceria reticulated porous foam, packed-bed ceria powder, and blend of ceria mixed with inert  $\text{Al}_2\text{O}_3$  particles),  $\text{CH}_4$  flow-rate, reduction temperature, and sintering temperature on the bed-averaged oxygen non-stoichiometry ( $\delta$ ), methane conversion, syngas production yield, and reactor performance was experimentally investigated and evaluated. A comprehensive experimental analysis of the solar process performance outputs was performed, encompassing quantification of gas yields produced during each step and by each side reaction, amounts of oxygen transferred during the redox process as well as energy conversion efficiencies. Besides, cycling stability of the ceria structure for the combined two-step process performed in this solar reactor was also assessed.

## **2. Experimental set up and methods**

The solar reactor design and auxiliary components are schematically shown in Fig. 1. The solar reactor concept is based on a directly-irradiated packed-bed solar absorber configuration. The metallic cavity receiver is cylindrical with a conical shape ( $60^\circ$  angle) at the cavity bottom (volume: 0.299 L and total height: 115 mm) and insulated by a 30 mm-thick alumino-silicate insulation layer. Its bottom is bored for the passage of an alumina tube (4x2 mm) in which argon (Ar) carrier gas, and either  $\text{CH}_4$  or  $\text{H}_2\text{O}/\text{CO}_2$  are fed to react with

ceria samples. The insulated cavity is vertically positioned in a water-cooled cylindrical stainless-steel shell. The top of the cavity is first closed by an alumina cap with a 20 mm-diameter aperture and then a protective graphite layer (2 mm-thick) with a 15 mm-diameter aperture. The reactor front is lastly sealed by a hemispherical transparent glass window. A 2-m parabolic dish solar concentrator with a solar concentration ratio up to 10,551 suns (peak flux density of  $\sim 10.5 \text{ MW/m}^2$  for a DNI of  $1 \text{ kW/m}^2$ ) is used to concentrate the solar radiation to the focal point.

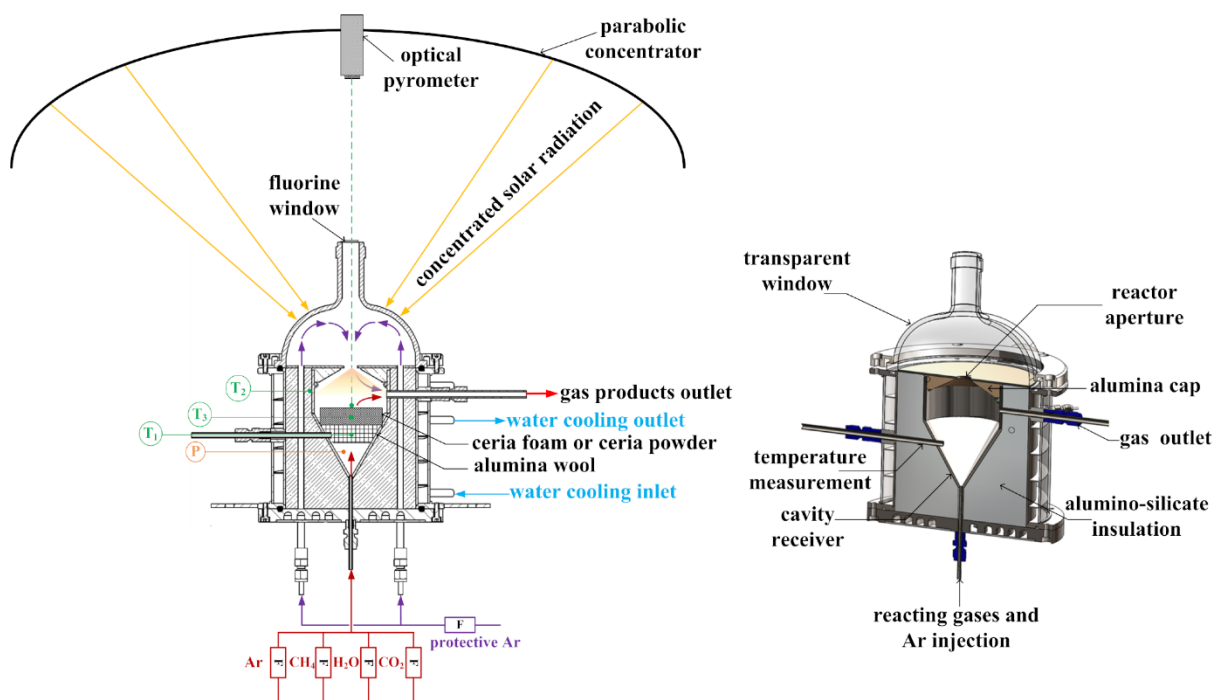


Fig. 1. Schematic of the  $1.5 \text{ kW}_{\text{th}}$  directly irradiated solar reactor and external components (left) and 3D cross section of the solar reactor (right).

Three temperatures are measured by B-type thermocouples inside the alumina wool ( $T_1$ ), in the middle of ceria structure ( $T_3$ ), and at the external cavity wall surface ( $T_2$ ). An optical pyrometer (operating at  $4.8\text{-}5.2 \mu\text{m}$  in a  $\text{H}_2\text{O}$  absorption band) is also utilized to directly measure the uppermost sample surface temperature through a fluorine window. The cavity pressure ( $P$ ) is measured by a pressure transducer. Samples, either loose particles or foam (Fig.S1), are placed on the alumina wool support inside the cavity receiver directly



exposed to concentrated solar irradiation. The ceria materials preparation is described in Supporting Information (materials synthesis). CH<sub>4</sub>, CO<sub>2</sub>, and Ar (gases purity of 99.999%) flow-rates are regulated by electronic Mass Flow Controllers (MFC, Brooks Instruments model SLA5850S, range 0-5 NI/min  $\pm$ 0.2% of full scale), and liquid water is also supplied by a MFC (range 0-30 g/h  $\pm$ 1% of full scale). Reacting gases and Ar carrier gas are injected through the single inlet port at the cavity bottom. In addition, Ar protective gas is fed directly into the window area by two stainless tubes inserted in the insulation layer and subsequently enters the cavity via the aperture in the downward direction for preventing the hot gas contact with the transparent window. All the product gases with Ar exit the reactor via a single outlet port positioned at the upper cylindrical part of the cavity. They subsequently flow into a bubbler to condense steam and then through a gas filtering unit (two micro filters with 0.1  $\mu$ m pore diameter) to remove moisture and solid carbon particles prior to gas analysis. Product syngas composition is monitored by an on-line syngas analyzer (GEIT 3100, uncertainty  $<\pm$ 0.1% of full scale). Finally, all the measured data are recorded by an automated data acquisition system (BECKHOFF).

Experiments were performed at the focus of a vertical axis high-flux solar furnace of CNRS-PROMES, Odeillo. The reactor cavity was primarily flushed with Ar and simultaneously sucked by a Venturi pump to purge residual air from the system and maintain the pressure at  $\sim$ 0.9 bar ( $P_{\text{atm}} = \sim$ 0.85 bar at site elevation 1,500 m above sea level). Subsequently, the reactor was progressively solar-heated to the targeted reduction temperature. The solar power input was controlled by means of shutter opening to adjust the operating temperature. During heating, the Ar carrier gas (0.2 NI/min) and Ar protective gas (2 NI/min) were supplied to the reactor cavity and window area, respectively. Fig.2 represents the evolution of temperatures and cavity pressure in the directly irradiated solar reactor during heating phase, ceria foam reduction with methane, and subsequent oxidation with H<sub>2</sub>O

at different operating cycle temperatures. While the cavity pressure remained stable (0.86 bar), the temperature increased gradually from the ambient temperature to the targeted temperature (1000 °C) for 35 min. It then changed in relation to endothermic and exothermic reactions and nominal operating cycle temperature defined, while the cavity pressure was constant (~0.9 bar) all over the cycles. The homogeneous temperature inside the ceria foam as well as the reactor cavity receiver was confirmed by narrow gaps between  $T_1$  (below the foam),  $T_3$  (inside the foam), and  $T_{\text{pyrometer}}$  (upper surface of the foam) while the external cavity wall temperature was ~150 °C lower than those temperatures.

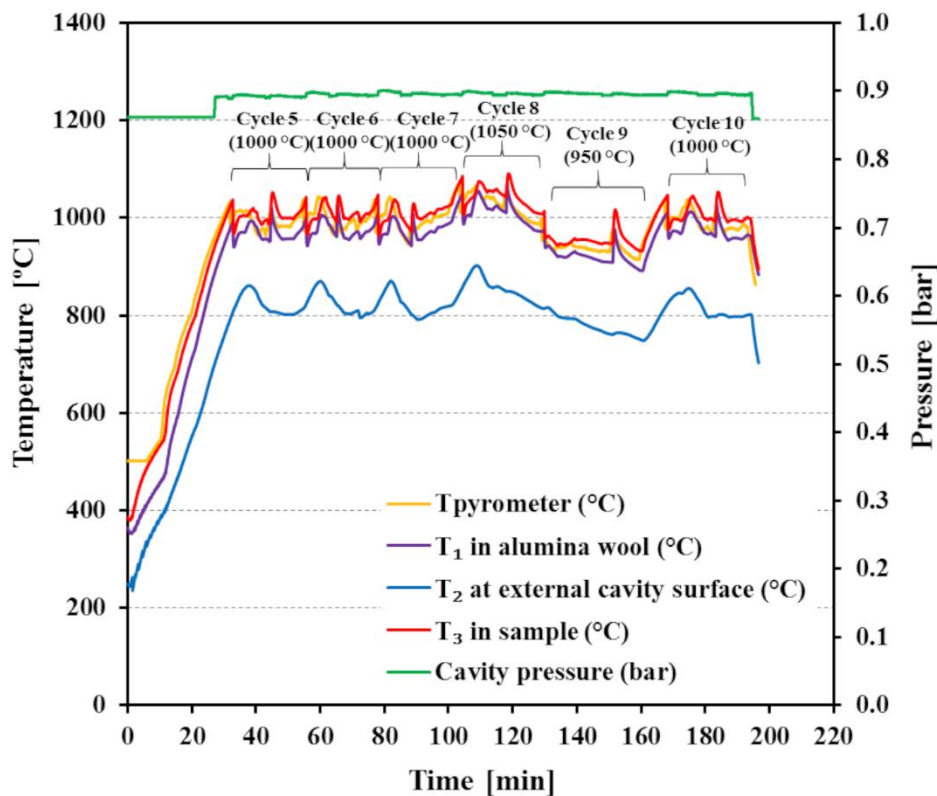


Fig. 2. Temperatures and pressure evolution in the reactor during heating phase, ceria foam reduction with methane and oxidation with  $\text{H}_2\text{O}$  (sample: ceria foam, ST-1000, 18.3705 g, cycles: 5-10 in Table S1).

After reaching the desired reduction temperature, the  $\text{CH}_4$  flow-rate was delivered along with Ar carrier gas to drive the reduction reaction, and it was then stopped when  $\text{H}_2$  and

CO concentrations approached zero. Subsequently, oxidation was performed by injecting the reacting gases (either H<sub>2</sub>O or CO<sub>2</sub>) at the same temperature. The produced syngas was continuously analyzed, and the flow rate of each gas specie ( $F_i$ ) was calculated from their measured mole fraction ( $y_i$ ) and the known inlet flow rate of Ar ( $F_{Ar}$ ): ( $F_i = F_{Ar} \cdot y_i / y_{Ar}$ ). Then, the averaged oxygen non-stoichiometry in ceria ( $\delta$ ) and syngas yields were quantified by time-integration of the measured gas production rates over each cycle. The performance metrics of the solar reactor were determined from the measured gas production and solar power input.

In the first step, during partial oxidation of methane with ceria, the reaction of CH<sub>4</sub> with excess surface oxygen is also possible (especially at the beginning of the reaction when the amount of surface oxygen is maximum), then leading to the formation of H<sub>2</sub>O and CO<sub>2</sub> (by the following reaction:  $4CeO_2 + \delta CH_4 \rightarrow 4CeO_{2-\delta} + \delta CO_2 + 2\delta H_2O$ ). Thus, oxygen is recovered in the forms of CO, CO<sub>2</sub>, and H<sub>2</sub>O (twice the amount of CO<sub>2</sub>). Therefore, the oxygen non-stoichiometry ( $\delta_{red}$ ) can be determined by:

$$\delta_{red} = \frac{n_{CO} + 2n_{CO_2} + n_{H_2O}}{n_{CeO_2}} \quad (4)$$

Where  $n_i$  are the mole amounts of species  $i$ .

The replenished oxygen ( $\delta_{ox}$ ) during ceria oxidation with H<sub>2</sub>O (Eq. (2)) can be calculated from the total amount of produced H<sub>2</sub> from which the amounts of H<sub>2</sub> produced by the reactions of carbon with H<sub>2</sub>O are subtracted (C+H<sub>2</sub>O→CO+H<sub>2</sub> and C+2H<sub>2</sub>O→CO<sub>2</sub>+2H<sub>2</sub>):

$$\delta_{ox} = \frac{n_{H_2} - n_{CO} - 2n_{CO_2}}{n_{CeO_2}} \quad (5)$$

When using CO<sub>2</sub> as oxidant (Eq. (3)), the replenished oxygen ( $\delta_{ox}$ ) is calculated by the mass balance of oxygen:

$$\delta_{ox} = \frac{2n_{CO_2,in} - n_{CO,out} - 2n_{CO_2,out}}{n_{CeO_2}} \quad (6)$$

The performance metrics of the solar reactor for the chemical-looping process are encompassing methane conversion, solar-to-fuel energy conversion efficiency, and energy upgrade factor.

The solar-to-fuel energy conversion efficiency ( $\eta_{\text{solar-to-fuel}}$ ) is defined as the ratio of the total chemical energy content of the produced syngas to the total energy input (including solar power input in both the reduction and oxidation steps and heating value of the converted methane):

$$\eta_{\text{solar-to-fuel}} = \frac{(\dot{m}_{\text{H}_2} \cdot \text{LHV}_{\text{H}_2} + \dot{m}_{\text{CO}} \cdot \text{LHV}_{\text{CO}})_{\text{cycle}}}{\dot{P}_{\text{solar}} + (X_{\text{CH}_4} \cdot \dot{m}_{\text{CH}_4} \cdot \text{LHV}_{\text{CH}_4})} \quad (7)$$

where  $\text{LHV}$  represents the Lower Heating Value (J/kg),  $\dot{m}_{\text{H}_2}$  and  $\dot{m}_{\text{CO}}$  the mass flow rates of  $\text{H}_2$  and  $\text{CO}$  produced in the cycle (kg/s),  $\dot{m}_{\text{CH}_4}$  the mass flow rate of injected methane,  $\dot{P}_{\text{solar}}$  the total solar power input in the cycle (W), and  $X_{\text{CH}_4}$  the methane conversion ( $X_{\text{CH}_4} = 1 - \frac{\dot{m}_{\text{unreacted CH}_4}}{\dot{m}_{\text{CH}_4}}$ ).

The energy upgrade factor (U) is obtained by the ratio of the energy contained in the outlet gas species to the energy content of the inlet flow:

$$U = \frac{(\dot{m}_{\text{H}_2} \cdot \text{LHV}_{\text{H}_2} + \dot{m}_{\text{CO}} \cdot \text{LHV}_{\text{CO}})_{\text{cycle}} + ((1 - X_{\text{CH}_4}) \cdot \dot{m}_{\text{CH}_4} \cdot \text{LHV}_{\text{CH}_4})}{(\dot{m}_{\text{CH}_4} \cdot \text{LHV}_{\text{CH}_4})} \quad (8)$$

All the operating conditions and experimental results for 44 runs with 6 different ceria samples performed in the solar reactor are summarized in Supporting Information (Table S1).

### 3. Results and discussion

#### 3.1 Influence of sintering temperature for ceria foams

In order to experimentally study the effect of calcination temperature during ceria foam elaboration on the evolved syngas yield, two ceria reticulated porous foams were prepared and subsequently annealed under air at 1000 °C (for 6 h) and one of them was further sintered at 1400 °C (for 2 h) for densifying the structure. Thus, the obtained sintered foams were labeled as ST-1000 and ST-1400, respectively. The initial volumes of ST-1000 and ST-1400 were 46.76 and 83.13 cm<sup>3</sup> (after ceria coating process), and they were shrunk to 30.88 cm<sup>3</sup> (Fig. 3a, ST-1000) and 31.10 cm<sup>3</sup> (Fig. 3b, ST-1400) after heat treatment, representing a decrease of 34% and 63% of their initial volume, respectively. The final properties of the ceria foams are: porosity: 91.8 and 89.1 %, mean cell size: 3.5 and 2.5 mm, and apparent density: 0.595 and 0.780 g/cm<sup>3</sup> for ST-1000 and ST-1400, respectively.

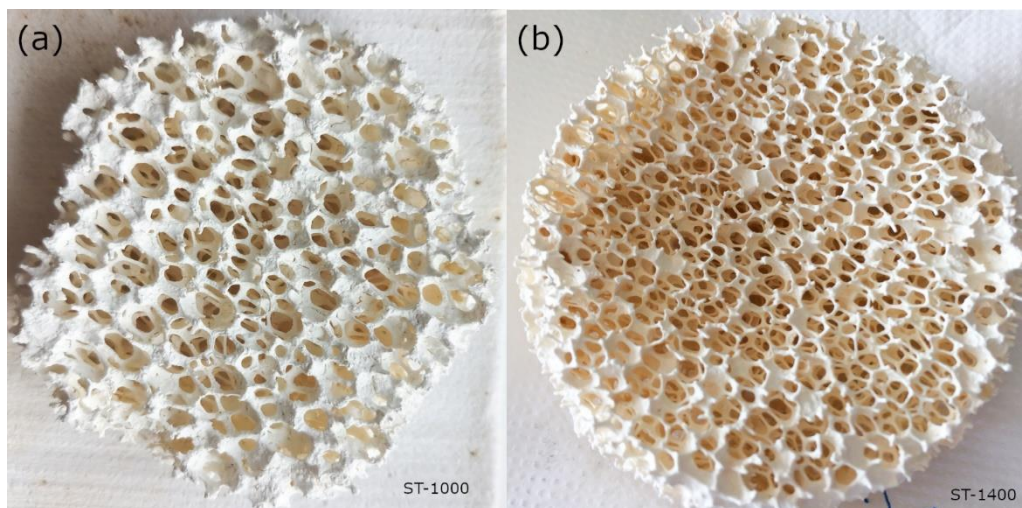


Fig. 3. Ceria reticulated foam fabricated for the solar cavity receiver: (a) after final heat treatment at 1000°C (13 mm thickness, 55 mm diameter) and (b) after final heat treatment at 1400°C (11 mm thickness, 60 mm diameter).

Both ceria foams were cycled in the temperature range 900-1050 °C to experimentally study the influence of temperature on syngas evolution as well as reactor performance.

Fig.4 shows the syngas production rate along with nominal reactor temperature during ceria foam reduction (ST-1400) in the range 900-1050 °C (CH<sub>4</sub> flow-rate: 0.2 NI/min, Ar

flow rate: 0.2 Nl/min, 50% CH<sub>4</sub> mole fraction). It was followed by subsequent ceria oxidation with H<sub>2</sub>O carried out at the same temperature (H<sub>2</sub>O: 200 mg/min, Ar: 0.2 Nl/min, 55% steam mole fraction at inlet).

During reduction step, CO<sub>2</sub> production rate was maximal at the initial stage of the reaction, and it increased with temperature. In fact, H<sub>2</sub>O was also formed simultaneously [9,10,42]; however, it cannot be detected from gas analysis. An increase in the operating cycle temperature promoted both the syngas production rate (especially H<sub>2</sub> and CO) and ceria reduction rate (as evidenced by a shortened reaction duration). The peak rates of CO and H<sub>2</sub> produced were 0.02 and 0.04 Nl/min at 900 °C compared to 0.11 and 0.24 Nl/min at 1050 °C, and the operating duration was 25.4 min at 900 °C compared to 18.4 min at 1050 °C. It is interesting to note that the H<sub>2</sub>/CO mole ratio is constantly ~2 for any reduction temperatures [9]. Moreover, the significant H<sub>2</sub> evolution still continuing after 12 min (Fig. 4e) was the result of the methane cracking reaction that is thermodynamically favorable at high temperature (>1000 °C) [23].

During oxidation step, the H<sub>2</sub> production rate increased with temperature while the CO and CO<sub>2</sub> production rates were negligible over the considered temperature range, thus demonstrating negligible impact of carbon formation associated with methane cracking for ST-1400.

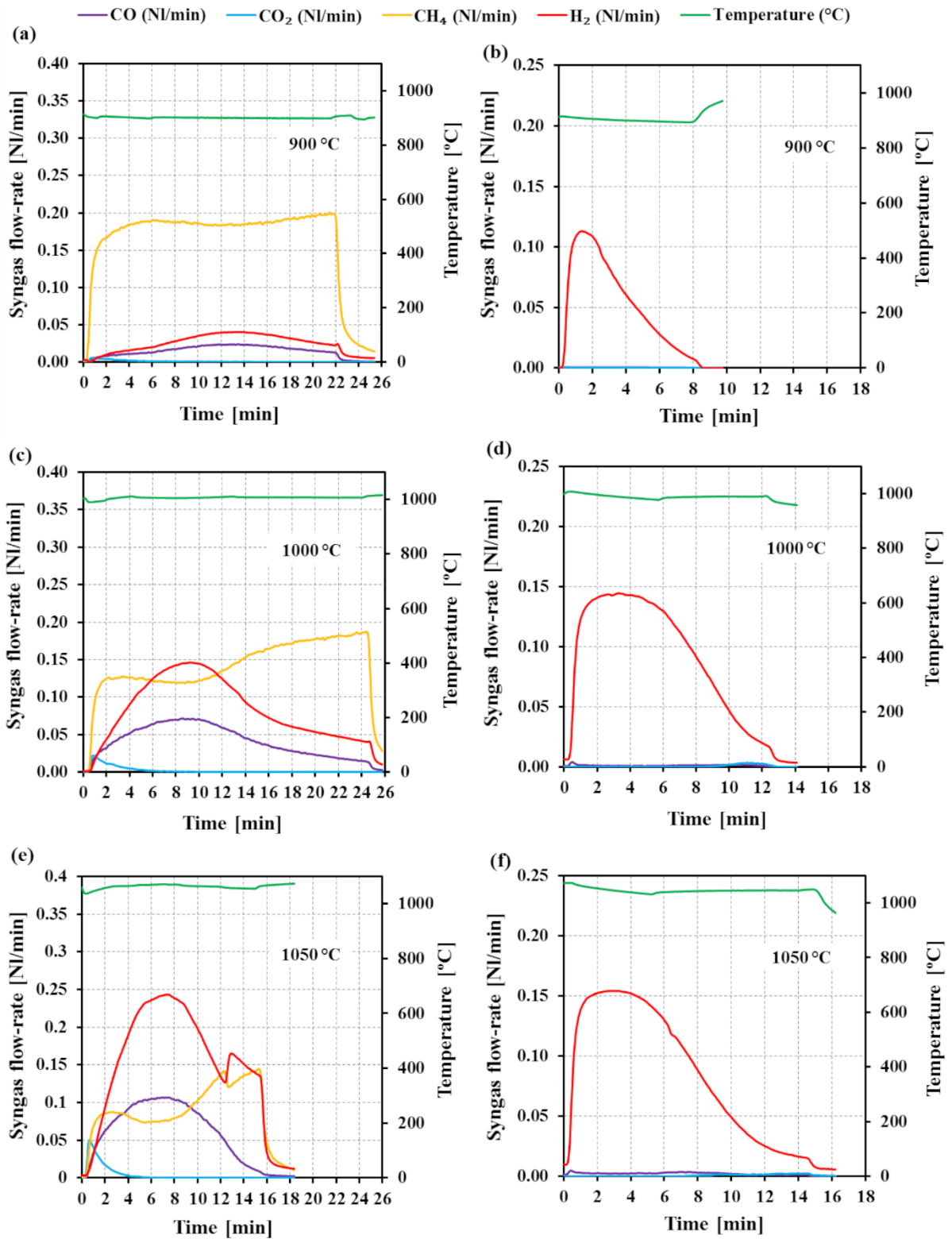


Fig. 4. Evolution of the production rates of H<sub>2</sub>, CO, CO<sub>2</sub> and CH<sub>4</sub> in the syngas along with nominal reactor temperature for reduction (a, c, and e) and oxidation (b, d, and f) of ceria foam (ST-1400) cycled isothermally at different temperatures.

Fig.5 compares the H<sub>2</sub>, CO, and CO<sub>2</sub> production rates (both reduction and oxidation steps) of ceria foam ST-1400 to those of ST-1000 at an operating cycle temperature of 1000 °C. During reduction step (Fig.5a), increasing the sintering temperature (ST-1400) decreased syngas production rates while increasing the operating duration. This is because the high densification of the structure (at high sintering temperature of 1400 °C) leads to a decline of the porosity and hinders the access of the reacting gas to the solid surface and hollow struts of the foam. Likewise, higher sintering temperature (ST-1400) also led to lower reaction rates during oxidation step (Fig.5b). Decreasing the sintering temperature (ST-1000) favored the oxidation rate and the formation of CO/CO<sub>2</sub> (because the formation of carbon during the reduction step was also favored).



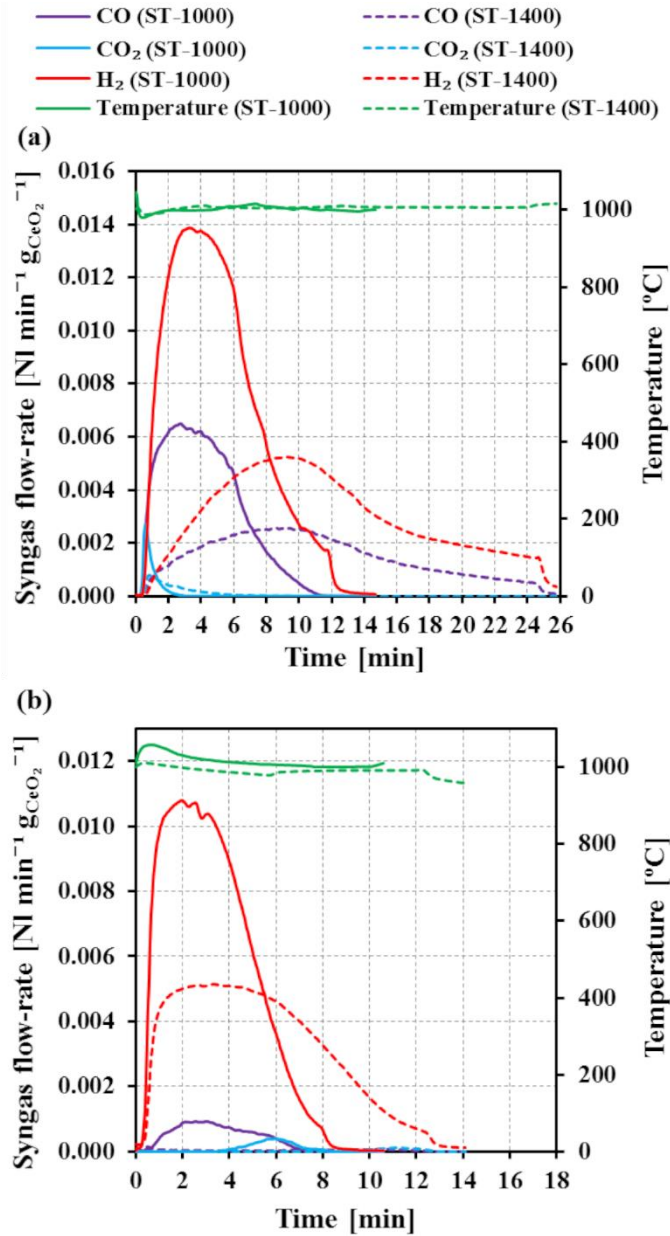


Fig. 5. Influence of sintering temperature on H<sub>2</sub> and CO production rates during both reduction and oxidation of ceria foam at 1000 °C: (a) CH<sub>4</sub> was utilized as reducing agent and (b) H<sub>2</sub>O was utilized as oxidizing agent.

Fig.6 presents the comparison of syngas yields (calculated by time-integration of the measured syngas production rates) produced per gram of CeO<sub>2</sub> [mmol/g<sub>CeO<sub>2</sub></sub>] between ST-1000 and ST-1400 at the operating cycle temperature of 1000 and 1050 °C during ceria reduction with CH<sub>4</sub> (Fig.6a) and oxidation with H<sub>2</sub>O (Fig.6b). The syngas yields ascribed to

the main reactions (Eqs.1 and 2) and side reactions (methane cracking during reduction step:  $\text{CH}_4 \rightarrow \text{C} + 2\text{H}_2$ , and carbon gasification during oxidation step:  $\text{C} + \text{H}_2\text{O} \rightarrow \text{CO} + \text{H}_2$  and  $\text{C} + 2\text{H}_2\text{O} \rightarrow \text{CO}_2 + 2\text{H}_2$ ) are presented separately.

Fig.6a shows that the syngas yields produced during reduction step decreased significantly with sintering temperature at the operating cycle temperatures of 1000 and 1050 °C, thus leading to a decline in  $\delta_{\text{red}}$  (e.g., from 0.36 for ST-1000 to 0.34 for ST-1400 at 1000 °C). Furthermore, the  $\text{H}_2$  yield produced from  $\text{CH}_4$  cracking reaction (quantified by the total  $\text{H}_2$  yield measured by gas analysis minus the  $\text{H}_2$  yield produced by the reaction of ceria with methane, which is equivalent to twice the quantity of produced CO, according to Eq.1) decreased considerably when increasing the sintering temperature (e.g. from 0.67 mmol/g $\text{CeO}_2$  for ST-1000 to 0.07 mmol/g $\text{CeO}_2$  for ST-1400 at 1000 °C). This can be explained by the fact that increasing the sintering temperature lowers the available geometrical surface area for the heterogeneous reaction, which declines the surface concentration of adsorbed methane and alleviates the methane cracking reaction.

Likewise, Fig.6b confirms that the methane cracking reaction is not favored for the sintered ceria foam (ST-1400), as evidenced by a sharp drop in the quantities of CO ( $\text{C} + \text{H}_2\text{O}$ ),  $\text{CO}_2$  ( $\text{C} + 2\text{H}_2\text{O}$ ),  $\text{H}_2$  ( $\text{C} + \text{H}_2\text{O}$ ), and  $\text{H}_2$  ( $\text{C} + 2\text{H}_2\text{O}$ ) formed by the side reactions (carbon deposit gasification with  $\text{H}_2\text{O}$ ). Note that the  $\text{H}_2$  ( $\text{C} + \text{H}_2\text{O}$ ) yield is equal to the CO yield measured by gas analysis ( $\text{C} + \text{H}_2\text{O} \rightarrow \text{CO} + \text{H}_2$ ), while the  $\text{H}_2$  ( $\text{C} + 2\text{H}_2\text{O}$ ) yield is equal to twice the  $\text{CO}_2$  yield measured by gas analysis ( $\text{C} + 2\text{H}_2\text{O} \rightarrow \text{CO}_2 + 2\text{H}_2$ ). In addition, an increase in the sintering temperature decreased the  $\text{H}_2$  ( $\text{CeO}_{2-\delta} + \text{H}_2\text{O}$ ) yield (e.g., from 2.04 mmol/g $\text{CeO}_2$  for ST-1000 to 1.84 mmol/g $\text{CeO}_2$  for ST-1400 at 1000 °C, then resulting in a decrease of  $\delta_{\text{ox}}$  from 0.35 to 0.32). Noticeably,  $\delta_{\text{red}}$  matched well  $\delta_{\text{ox}}$  values at both cycle temperatures of 1000 and 1050 °C, thereby confirming complete re-oxidation.

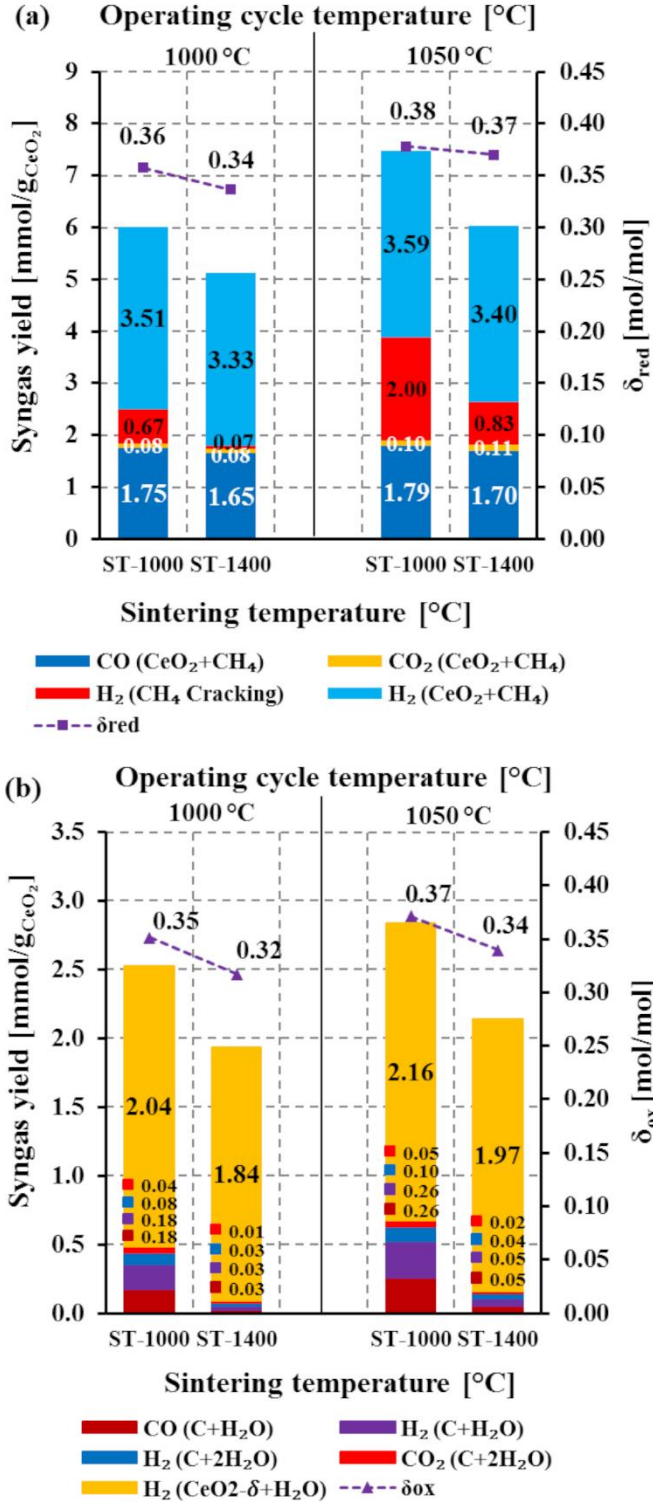


Fig. 6. Effect of sintering temperature and cycle operating temperatures on syngas yields,  $\delta_{red}$ , and  $\delta_{ox}$  for (a) reduction and (b) oxidation of ceria foam cycled isothermally at a CH<sub>4</sub> flow-rate of 0.2 Nl/min.

According to Fig 7a, the reduction yield ( $X_{\text{red}}=\delta_{\text{red}}/\delta_{\text{max}}$  where  $\delta_{\text{max}}=0.5$  for complete reduction of  $\text{Ce}^{4+}$  into  $\text{Ce}^{3+}$ ), oxidation yield ( $X_{\text{ox}}=\delta_{\text{ox}}/\delta_{\text{red}}$ ), methane conversion ( $X_{\text{CH}_4}$ ) and solar-to fuel energy conversion efficiency ( $\eta_{\text{solar-to-fuel}}$ ) were decreased when increasing the sintering temperature (e.g.,  $X_{\text{red}}$ ,  $X_{\text{ox}}$ ,  $X_{\text{CH}_4}$ , and  $\eta_{\text{solar-to-fuel}}$  ranging from 71.5%, 98.3%, 46.9%, and 3.8% for ST-1000 to 67.3%, 94.2%, 23.0%, and 2.8% for ST-1400, respectively, during cycling at 1000°C). In addition, an increase in operating cycle temperature enhanced  $X_{\text{red}}$ ,  $X_{\text{CH}_4}$ , and  $\eta_{\text{solar-to-fuel}}$ .

Fig.7b compares the total syngas yields obtained for both reduction and oxidation steps of ceria foams (ST-1000 compared to ST-1400) during cycling at 1000 and 1050 °C. Increasing sintering temperature considerably decreased total  $\text{H}_2$  and CO yields (from 6.48 and 1.93 mmol/g $_{\text{CeO}_2}$  for ST-1000<sub>2</sub> to 5.29 and 1.68 mmol/g $_{\text{CeO}_2}$  for ST-1400, respectively, at 1000 °C); however, the  $\text{CO}_2$  and  $\text{H}_2\text{O}$  yields tended to decrease slightly. A growth in the energy upgrade factor (U) with increasing sintering temperature was observed (e.g., from 1.03 for ST-1000 to 1.08 for ST-1400). This is because a high sintering of the ceria foam lowers the gaseous reactant access to the reactive surface and the ceria bulk reduction, thus increasing the unreacted  $\text{CH}_4$  (much lower  $X_{\text{CH}_4}$  for ST-1400, Fig. 7a) and thereby leading to an increase in U. From these observations, it can be summarized that decreasing sintering temperature enhanced syngas selectivity; however, at the expense of weakened structure, with reduced thermo-mechanical resistance.

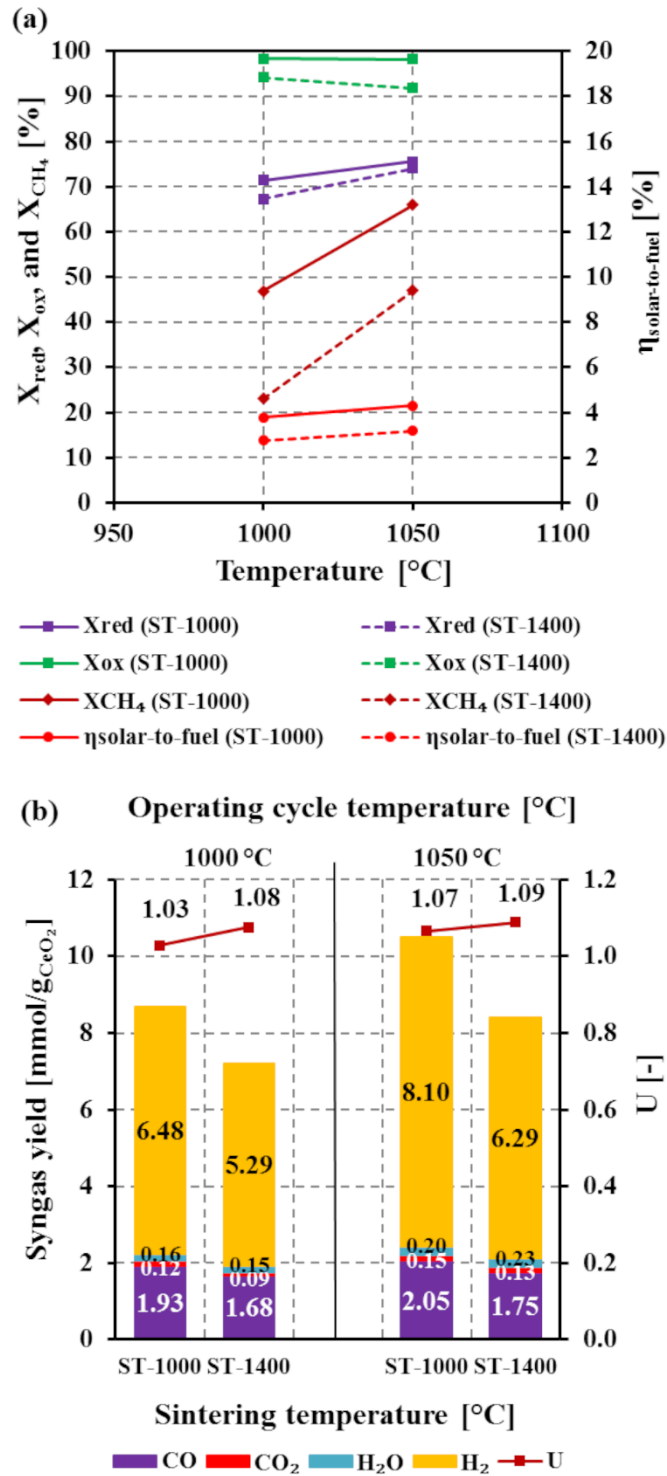


Fig. 7. Effect of sintering temperature and cycle operating temperatures on (a) ceria reduction yield, ceria oxidation yield, methane conversion, and solar-to-fuel energy conversion efficiency, and (b) energy upgrade factor and total syngas yields obtained from both reduction and oxidation steps.

### 3.2 Influence of methane flow-rate and ceria macrostructure on syngas yield

The impact of methane flow-rate on syngas yields was experimentally studied with different ceria structures. Three ceria structures consisting of pure ceria powder (25.0052 g, bulk density: 1.12 g/cm<sup>3</sup>, loose bed porosity: 84.5%), ceria powder (27.0605 g) mixed with inert Al<sub>2</sub>O<sub>3</sub> promoter (bulk mixture density: 1.53 g/cm<sup>3</sup>, loose bed porosity: 69.1%), and ceria reticulated foam (18.3705 g, ST-1000, bulk density: 0.595 g/cm<sup>3</sup>, porosity: 91.8%) were employed to investigate the influence of ceria structure and reactive bed layout on syngas yield and reactor performance. During ceria reduction step, the CH<sub>4</sub> flow-rate was injected at 0.1, 0.2, 0.3 and 0.4 NI/min (with constant Ar carrier flow of 0.2 NI/min) at 1000 °C. In the oxidation step performed at the same temperature (1000 °C), H<sub>2</sub>O was delivered at a constant flow-rate of 200 mg/min (with Ar carrier gas flow of 0.2 NI/min).

Fig. 8 shows the influence of CH<sub>4</sub> flow rate on syngas yields for each ceria structure. According to Fig.8a, the H<sub>2</sub> and CO yields first increased significantly within a CH<sub>4</sub> flow-rate range of 0.1-0.2 NI/min and then tended to grow minimally at above 0.2 NI/min. For example, the H<sub>2</sub> and CO yields for ceria foam rose from 3.25 and 1.66 mmol/g<sub>CeO<sub>2</sub></sub> at 0.1 NI/min to 3.64 and 1.82 mmol/g<sub>CeO<sub>2</sub></sub> at 0.2 NI/min, and 3.78 and 1.89 mmol/g<sub>CeO<sub>2</sub></sub> at 0.4 NI/min. The CO<sub>2</sub> yields for each ceria structure remained stable in negligible amounts (0.05-0.10 mmol/g<sub>CeO<sub>2</sub></sub> within the considered range). A plateau in the H<sub>2</sub> and CO (at CH<sub>4</sub> above 0.2 NI/min) indicates that the final state completion of ceria reduction for each ceria structure is being approached, thereby leading to an excess in CH<sub>4</sub> flow-rate supply, which in turn favors CH<sub>4</sub> cracking reaction. Note that if the rate of ceria reduction is lower than the rate of methane decomposition, chemisorbed carbon may accumulate at the surface. This occurs when the rate of bulk lattice oxygen diffusion to the surface becomes lower than the CH<sub>4</sub> supply rate. In other words, when a lack of oxygen at the surface occurs, then carbon deposition is fastened, which is increasingly favored as oxygen is being depleted during the

ceria reduction progress. It is interesting to highlight that when accounting for H<sub>2</sub> produced by CH<sub>4</sub> cracking reaction (Fig.8b), the H<sub>2</sub> yield increased steeply (3.25-6.54 mmol/g<sub>CeO<sub>2</sub></sub> for ceria foam) over the considered range, thus confirming that the CH<sub>4</sub> cracking reaction is favored when increasing CH<sub>4</sub> flow-rate, thus leading to a sharp increase in H<sub>2</sub> yield along with carbon deposition.

The CO and H<sub>2</sub> productions for each ceria structure were not significantly different, although a slightly higher H<sub>2</sub> and CO production was noticed for ceria powder (presumably due to non-uniform heating of the bed ( $T_{\text{pyrometer}} > T_3$ ) as evidenced by Fig. S2 for ceria powder and Fig. S3 for ceria powder mixed with inert Al<sub>2</sub>O<sub>3</sub> promoter). This advantageously confirms that the shaping of ceria as foam does not downgrade the reactivity.

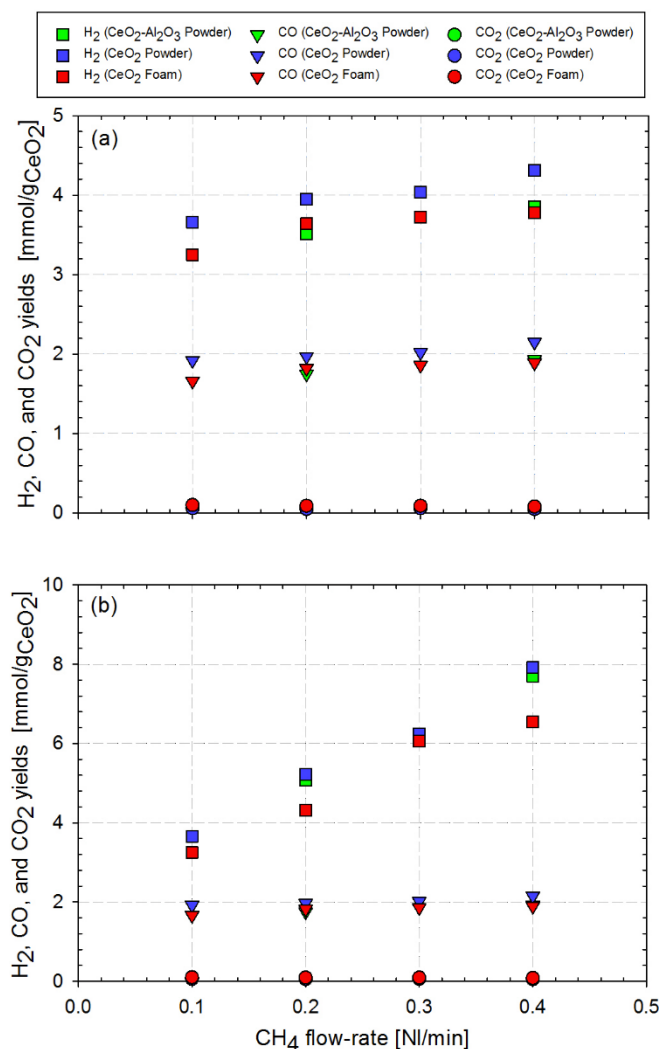


Fig. 8. Effect of CH<sub>4</sub> flow-rate on H<sub>2</sub> and CO yields during reduction of different ceria structures at 1000 °C: (a) not accounting and (b) accounting for H<sub>2</sub> produced by CH<sub>4</sub> cracking reaction.

During subsequent ceria oxidation with H<sub>2</sub>O at 1000 °C (Fig. 9), H<sub>2</sub> yield (produced by Eq. 2) increased in accordance with an increase in CH<sub>4</sub> flow-rate during the reduction step, while the CO and CO<sub>2</sub> yields (produced by side reactions) also rose due to carbon deposition increase (Fig. 9a). For instance, the yields of H<sub>2</sub>, CO, and CO<sub>2</sub> for ceria foam were 2.01, 0.11, and 0.01 mmol/g<sub>CeO<sub>2</sub></sub> at 0.1 NI/min compared to 2.16, 0.20, and 0.04 mmol/g<sub>CeO<sub>2</sub></sub> at 0.4 NI/min. Likewise, the H<sub>2</sub> yield increased sharper when including the amount of H<sub>2</sub> associated with carbon gasification (e.g. from 2.14 to 2.45 mmol/g<sub>CeO<sub>2</sub></sub> at 0.1-0.4 NI/min for ceria foam), according to Fig. 9b. However, no significant effect of the ceria structure on H<sub>2</sub>, CO, and CO<sub>2</sub> yields can be evidenced whether or not accounting for H<sub>2</sub> yields from carbon gasification reactions.



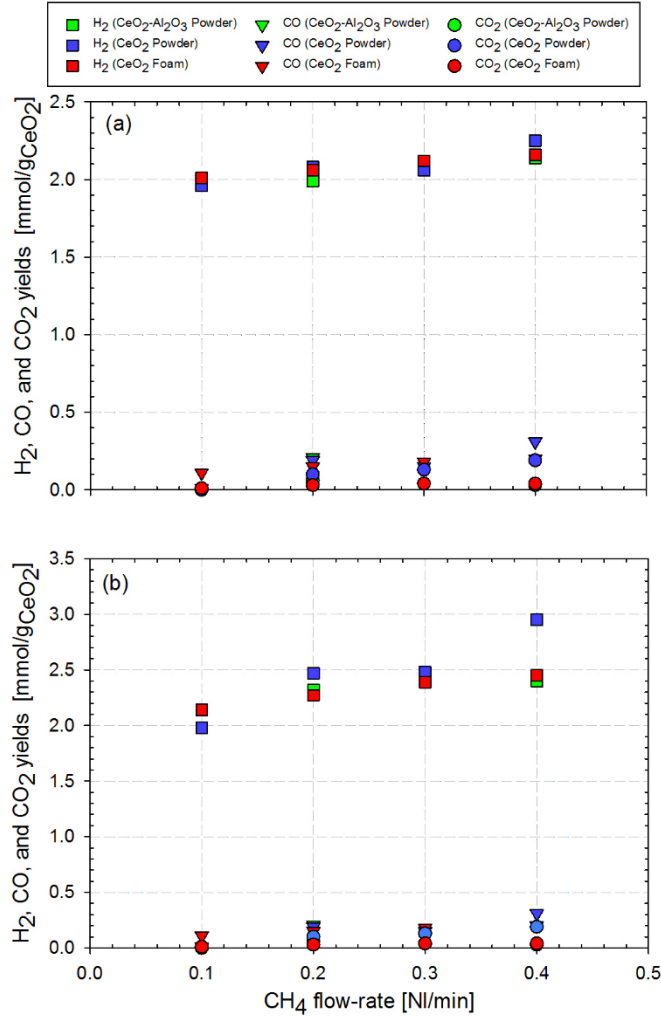


Fig. 9. Effect of  $\text{CH}_4$  flow-rate on  $\text{H}_2$  and  $\text{CO}$  yields during oxidation of different ceria structures with  $\text{H}_2\text{O}$  at  $1000\text{ }^\circ\text{C}$ : (a) not accounting and (b) accounting for  $\text{H}_2$  produced by carbon gasification reactions.

In order to emphasize the influence of  $\text{CH}_4$  flow-rate on reactor performance, the evolution of the relevant metrics ( $\delta_{\text{red}}$  and  $\delta_{\text{ox}}$ ,  $X_{\text{red}}$ ,  $X_{\text{ox}}$ ,  $X_{\text{CH}_4}$ ,  $U$ , and  $\eta_{\text{solar-to-fuel}}$ ) is presented in Fig.10. Both  $\delta_{\text{red}}$  (Fig.10a) and  $\delta_{\text{ox}}$  (Fig.10b) are enhanced with a  $\text{CH}_4$  flow-rate increase (e.g., maximum  $\delta_{\text{red}}$  and  $\delta_{\text{ox}}$  of 0.41 and 0.39 at 0.4 NI/min, respectively, for ceria powder). Besides, the  $\delta_{\text{ox}}$  values were consistent with  $\delta_{\text{red}}$  for any ceria structures, thereby confirming complete ceria re-oxidation with  $\text{H}_2\text{O}$ . As expected, the  $\delta_{\text{red}}$  (Fig.10a) of ceria powder (0.37-0.41) was slightly higher than those of other materials, in agreement with the higher syngas

yields during reduction (Fig. 8). The  $\delta_{ox}$  values were not different (Fig.10b) (0.34-0.39 for ceria powder and 0.35-0.37 for ceria reticulated foam), in agreement with the similar syngas yields during oxidation (Fig. 9).  $X_{red}$  grew with increasing  $CH_4$  flow-rate (Fig.10c), e.g. from 74.7% at 0.1 NI/min to 81.3% at 0.4 NI/min for ceria powder, and no significant influence of ceria structure on  $X_{red}$  can be observed.  $X_{ox}$  values were close to ~100% for any ceria structures, thereby demonstrating complete ceria re-oxidation.  $X_{CH_4}$  was reduced noticeably with increasing  $CH_4$  flow-rate for each ceria structure (Fig.10d) (e.g., from 76.4 to 43.0% at 0.1-0.4 NI/min, respectively, for ceria powder). The decrease in  $X_{CH_4}$  is attributable to the  $CH_4$  supply rate that exceeds the rate of oxygen released by ceria, as noticed by a stable profile in  $X_{red}$  at 0.3-0.4 NI/min (Fig.10c).  $U$  tended to decrease with  $CH_4$  flow-rate (Fig.10e). This variation is attributed to the carbon formation increase with  $CH_4$  flow-rate, and partial entrainment out of the reactor cavity, as confirmed by the presence of carbon particles in the filtering unit (Fig.S4), thus losing their heating value and lowering  $U$ . As expected,  $\eta_{solar-to-fuel}$  rose with  $CH_4$  flow-rate as a result of the substantial syngas yield improvement (Figs.8 and 9), and the highest  $\eta_{solar-to-fuel}$  was obtained for ceria foam (3.1-5.6%), followed by  $CeO_2$ - $Al_2O_3$  blend (3.6-5.0%), and  $CeO_2$  powder (3.1-3.6%), according to Fig.10f. This can be explained by the different solar power inputs required for different ceria structures (1.06-1.14 kW for ceria powder, followed by 0.96-1.06 kW for  $CeO_2$ - $Al_2O_3$  blend, and 0.76-0.86 kW for ceria foam). Ceria foam thus requires lower solar power consumption than  $CeO_2$ - $Al_2O_3$  blend and  $CeO_2$  powder. This is because the  $CeO_2$ - $Al_2O_3$  blend stands out from its high bed thickness (1.19 cm) and additional  $Al_2O_3$  heating (Fig.S5), while the  $CeO_2$  powder layer (0.46 cm thickness) shows high opacity, which is not suitable for efficient radiative heat transfer in the whole volume. Both issues thus lead to temperature gradient, as evidenced in both Fig.S2 (for  $CeO_2$  powder) and Fig.S3 (for  $CeO_2$ - $Al_2O_3$  blend), with a higher temperature at the bed uppermost surface ( $T_{pyrometer} > T_3$ ). However, the  $CeO_2$ - $Al_2O_3$  blend offers a favored

dispersion of ceria powder, which improves the gas flow through the reactive bed and heat transfer, and promotes the syngas yield (thereby leading to higher  $\eta_{\text{solar-to-fuel}}$  than for ceria powder). The ceria foam consumed the lowest solar power input (thus enhancing  $\eta_{\text{solar-to-fuel}}$ ), arising from the effective heat transfer through the semi-transparent medium and the uniform heating (as evidenced by the narrow temperature gap between ceria surface  $T_{\text{pyrometer}}$  and  $T_3$  in Fig. 2). In summary, the ceria foam structure is the most efficient in term of heat transfer (as reflected by uniform heating with lower solar power consumption), thereby leading to higher  $\eta_{\text{solar-to-fuel}}$ , and it is thus the most suitable for the chemical-looping methane reforming.

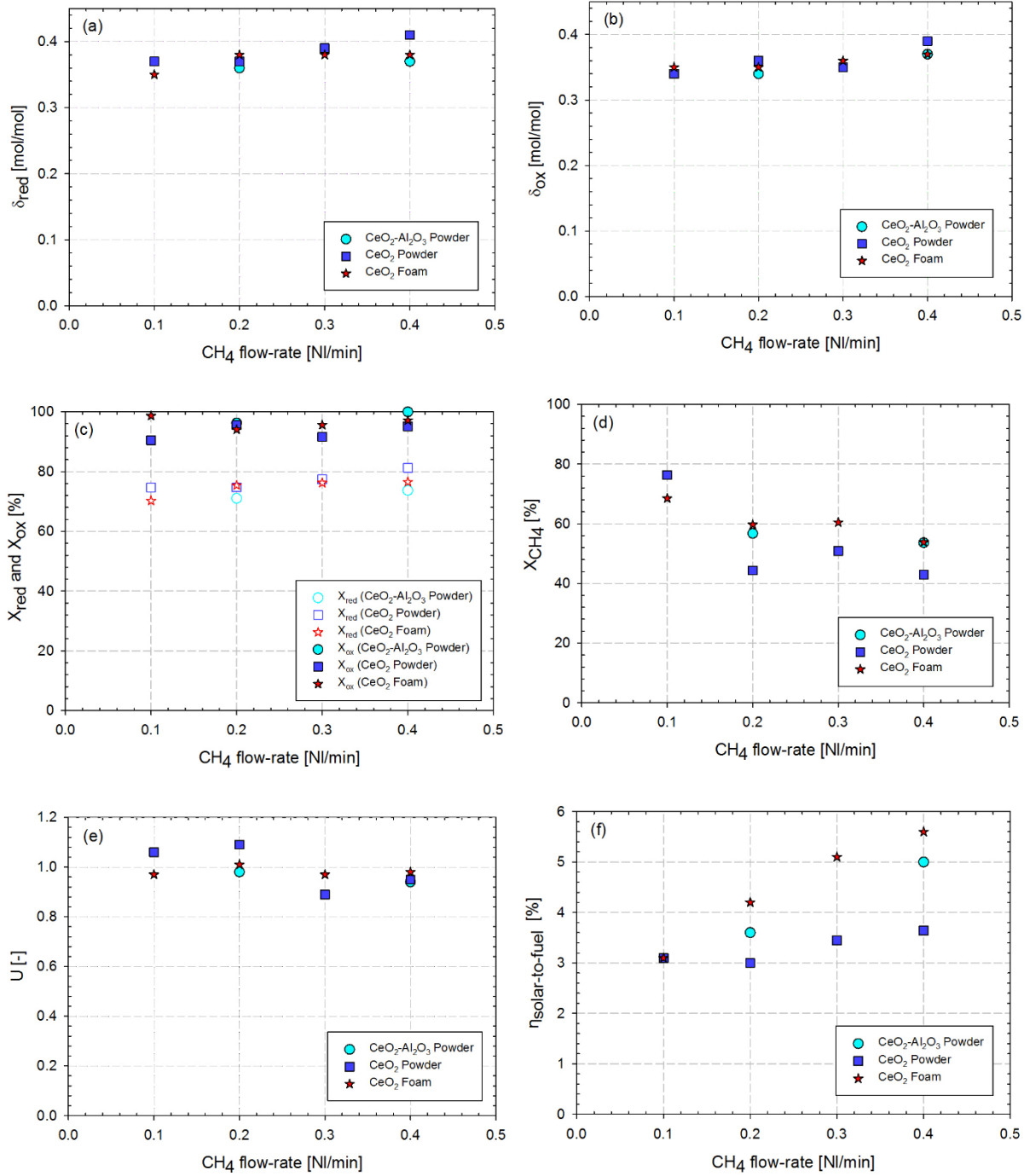


Fig. 10. Effect of CH<sub>4</sub> flow-rate on (a)  $\delta_{red}$ , (b)  $\delta_{ox}$ , (c) reduction yield ( $X_{red}$ ) and oxidation yield ( $X_{ox}$ ), (d) CH<sub>4</sub> conversion ( $X_{CH_4}$ ), (e) energy upgrade factor ( $U$ ), and (d) solar-to-fuel energy conversion efficiency ( $\eta_{solar-to-fuel}$ ) for different ceria structures at 1000 °C.

### 3.3 Influence of temperature on syngas yield

The influence of temperature on syngas yield was investigated for the different ceria structures at 900, 950, 1000, and 1050 °C ( $T_3$  is the nominal-mentioned temperature for experiments).

Fig. 11 shows the  $H_2$ , CO, and  $CO_2$  yields obtained from ceria reduction with  $CH_4$  as a function of reduction temperature. As expected, both  $H_2$  and CO yields increased sharply, while  $CO_2$  tended to rise minimally with temperature (Fig. 11a), regardless of the ceria structures. For example,  $H_2$ , CO, and  $CO_2$  yields rose from 2.38, 1.21, and 0.05 mmol/ $g_{CeO_2}$  at 900 °C to 3.84, 1.92, and 0.09 mmol/ $g_{CeO_2}$  at 1050 °C, respectively, for  $CeO_2-Al_2O_3$  blend. This is because increasing temperature accelerates the kinetic rate of ceria reduction with faster oxygen release, as evidenced by Arrhenius plot (Fig. S6). The activation energy obtained for each ceria structure (92.8-114.2 kJ/mol for  $H_2$  and 92.8-95.1 kJ/mol for CO, Table. S2) is consistent with previously reported data [23]. When accounting for the  $H_2$  produced by  $CH_4$  cracking reaction (Fig. 11b), the trends of  $H_2$  became steeper, thus pointing out the significant influence of the reduction temperature on the  $H_2$  formation from  $CH_4$  cracking. Noticeably, the  $H_2$  yield at 900 °C ( $CeO_2-Al_2O_3$  blend) remained the same (2.38 mmol/ $g_{CeO_2}$ ) whether or not accounting for  $H_2$  produced by cracking reaction, thus indicating that  $CH_4$  decomposition was negligible at 900 °C. In comparison, the ceria powder showed the highest  $H_2$  and CO yields at 950-1000 °C, as a result of the higher bed surface temperature and lower bed height, as previously mentioned.

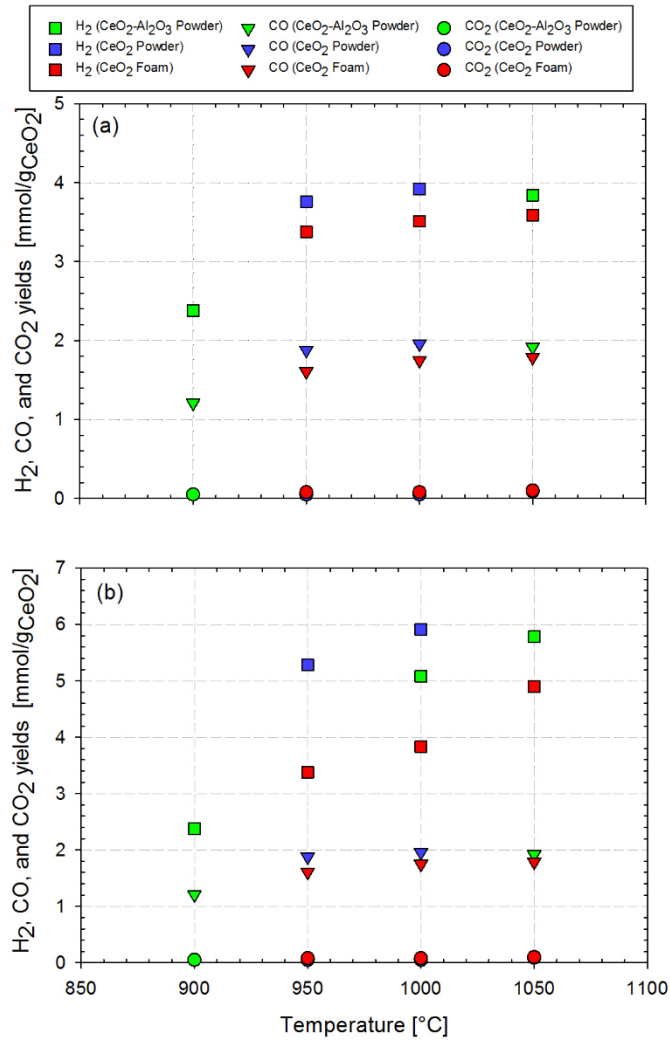


Fig. 11. Effect of temperature on H<sub>2</sub> and CO yields during ceria materials reduction with CH<sub>4</sub> (0.2 Nl/min, inlet CH<sub>4</sub> mole fraction: 50%): (a) not accounting and (b) accounting for H<sub>2</sub> produced by CH<sub>4</sub> cracking reaction.

Fig.12 depicts the H<sub>2</sub>, CO, and CO<sub>2</sub> yields measured during ceria oxidation with H<sub>2</sub>O as a function of temperature. The H<sub>2</sub> yields (from Eq.2) rose significantly with temperature (1.39-2.12 mmol/gCeO<sub>2</sub>, for CeO<sub>2</sub>-Al<sub>2</sub>O<sub>3</sub> blend), while a slight increase in CO and CO<sub>2</sub> yields was noticed (Fig.12a). The presence of CO and CO<sub>2</sub> (e.g., ranging between 0.06-0.23 for CO and 0.01-0.03 mmol/gCeO<sub>2</sub>, for CeO<sub>2</sub>-Al<sub>2</sub>O<sub>3</sub> blend) is attributed to the side reactions of carbon gasification forming additional H<sub>2</sub>, CO, and CO<sub>2</sub>. These side reactions are beneficial to eliminate the deposited carbon on the surface of ceria structure, thereby avoiding

deactivation. When including the H<sub>2</sub> produced by the carbon gasification (Fig.12b), the H<sub>2</sub> yield for each ceria structure was higher (1.46-2.40 mmol/g<sub>CeO<sub>2</sub></sub> for CeO<sub>2</sub>-Al<sub>2</sub>O<sub>3</sub> blend), thus confirming the growing effect of temperature on carbon formation.

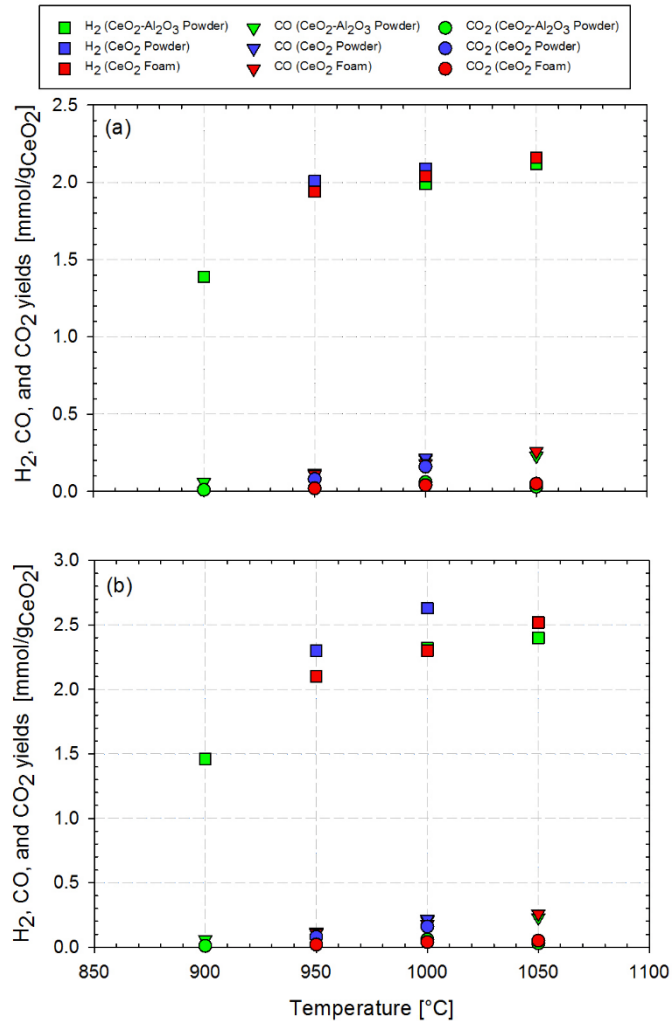


Fig. 12. Effect of temperature on H<sub>2</sub> and CO yields during ceria materials oxidation with H<sub>2</sub>O (200 mg/min, inlet steam mole fraction: 55%): (a) not accounting and (b) accounting for H<sub>2</sub> produced by carbon gasification reactions.

Fig.13 presents the evolution of  $\delta_{\text{red}}$ ,  $\delta_{\text{ox}}$ ,  $X_{\text{red}}$ ,  $X_{\text{ox}}$ ,  $X_{\text{CH}_4}$ ,  $U$ , and  $\eta_{\text{solar-to-fuel}}$  as a function of temperature for each ceria structure. The temperature increase improved steadily the reduction extent of ceria  $\delta_{\text{red}}$  (Fig 13a), e.g. from 0.24 at 950 °C to 0.39 at 1050 °C for CeO<sub>2</sub>-Al<sub>2</sub>O<sub>3</sub> blend owing to a significant beneficial enhancement of the reduction kinetics (Fig. S6).

$\delta_{\text{ox}}$  also increased with temperature (ranging between 0.24-0.36 for  $\text{CeO}_2\text{-Al}_2\text{O}_3$  blend, Fig.13b) due to the oxygen vacancies consistently increasing with temperature. The impact of the considered ceria structures on both  $\delta_{\text{red}}$  and  $\delta_{\text{ox}}$  was not significant.  $\delta_{\text{ox}}$  values were similar to  $\delta_{\text{red}}$  values, thus validating complete ceria re-oxidation for any ceria structures.  $X_{\text{red}}$  rose considerably with temperature (e.g., in the range 48.8-78.0% for  $\text{CeO}_2\text{-Al}_2\text{O}_3$  blend), while  $X_{\text{ox}}$  remained quite constant at  $\sim 100\%$  for any ceria structures (Fig.13c), thereby confirming complete ceria re-oxidation.  $X_{\text{CH}_4}$  rose with temperature (Fig.13d), and the highest  $X_{\text{CH}_4}$  was attained at 1050 °C (77.4% for  $\text{CeO}_2\text{-Al}_2\text{O}_3$  blend). This is because the faster rate of oxygen release better matched the constant inlet flow of  $\text{CH}_4$ , which leads to  $X_{\text{CH}_4}$  increase. The  $X_{\text{CH}_4}$  for both ceria foam and  $\text{CeO}_2\text{-Al}_2\text{O}_3$  blend was higher than that of ceria powder, presumably due to both better gas flow through the structure and solid/gas contact between ceria and  $\text{CH}_4$ . Moreover, U (Fig.13e) first increased slightly within 900-950 °C and then decreased above 950 °C, as a result of carbon formation issue. Indeed, the carbon deposition increased with increasing temperature, and some particles escaped from the reactor cavity via gas flow, thus lowering U. This issue can be tackled by decreasing temperature to favor U at the expense of lower syngas yield.  $\eta_{\text{solar-to-fuel}}$  (Fig.13f) was improved by increasing temperature (e.g., in the range of 3.0-4.3% for ceria foam). The lowest  $\eta_{\text{solar-to-fuel}}$  values were observed for ceria powder (2.75-2.97% at 950-1000 °C) because of the higher solar power consumption (0.88-0.96 kW for ceria powder compared to 0.67-0.68 kW for ceria foam in the temperature range 950-1000 °C), confirming that ceria foam structure is the most suitable for the solar combined process.



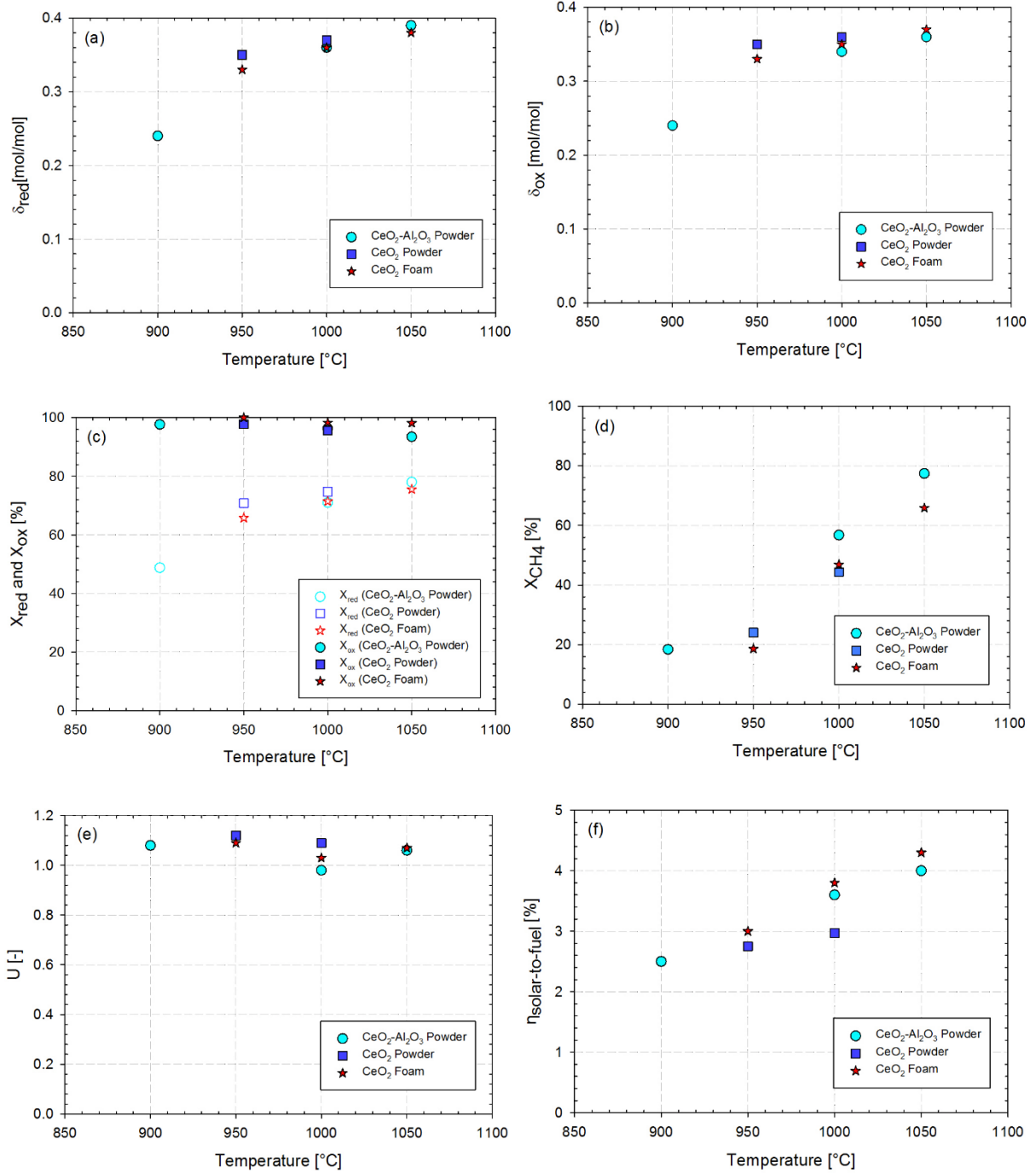


Fig. 13. Effect of temperature on (a)  $\delta_{red}$ , (b)  $\delta_{ox}$ , (c) reduction yield ( $X_{red}$ ) and oxidation yield ( $X_{ox}$ ), (d) CH<sub>4</sub> conversion ( $X_{CH_4}$ ), (e) energy upgrade factor ( $U$ ), and (d) solar-to-fuel energy conversion efficiency ( $\eta_{solar-to-fuel}$ ) for different ceria structures.

### 3.4 Oxidation step with CO<sub>2</sub> during ceria cycling

Another ceria powder (27.0892 g) mixed with  $\text{Al}_2\text{O}_3$  (50 g) was employed to study the influence of temperature (950-1050 °C) on syngas yield and reactor performance during ceria oxidation with  $\text{CO}_2$ . This ceria was first reduced with a constant  $\text{CH}_4$  flow-rate of 0.2 NI/min (50%  $\text{CH}_4$  mole fraction at inlet) and subsequently re-oxidized with a constant  $\text{CO}_2$  flow-rate of 0.2 NI/min (50%  $\text{CO}_2$  mole fraction at inlet) at the same temperature.

Syngas production rates along with reactor temperature for both steps are presented in Fig. 14. During reduction step, the syngas production rates were higher at 1050 °C than at 1000 and 950 °C. For instance, the peak  $\text{H}_2$  and  $\text{CO}$  production rates were 0.32 and 0.14 NI/min at 1050 °C compared to 0.21 and 0.10 NI/min at 950 °C. The reaction duration declined considerably with increasing temperature due to improved ceria reduction kinetics (from 24.4 min at 950 °C to 15.1 min at 1050 °C). During oxidation step, the peak  $\text{CO}$  production rate increased minimally from 0.14 to 0.16 NI/min while the oxidation duration decreased slightly (from 26 min at 950 °C to 22 min at 1050 °C). Therefore, the effect of temperature is not significant for the oxidation step with  $\text{CO}_2$ , which thus suggests low impact of kinetic reaction control for this step.

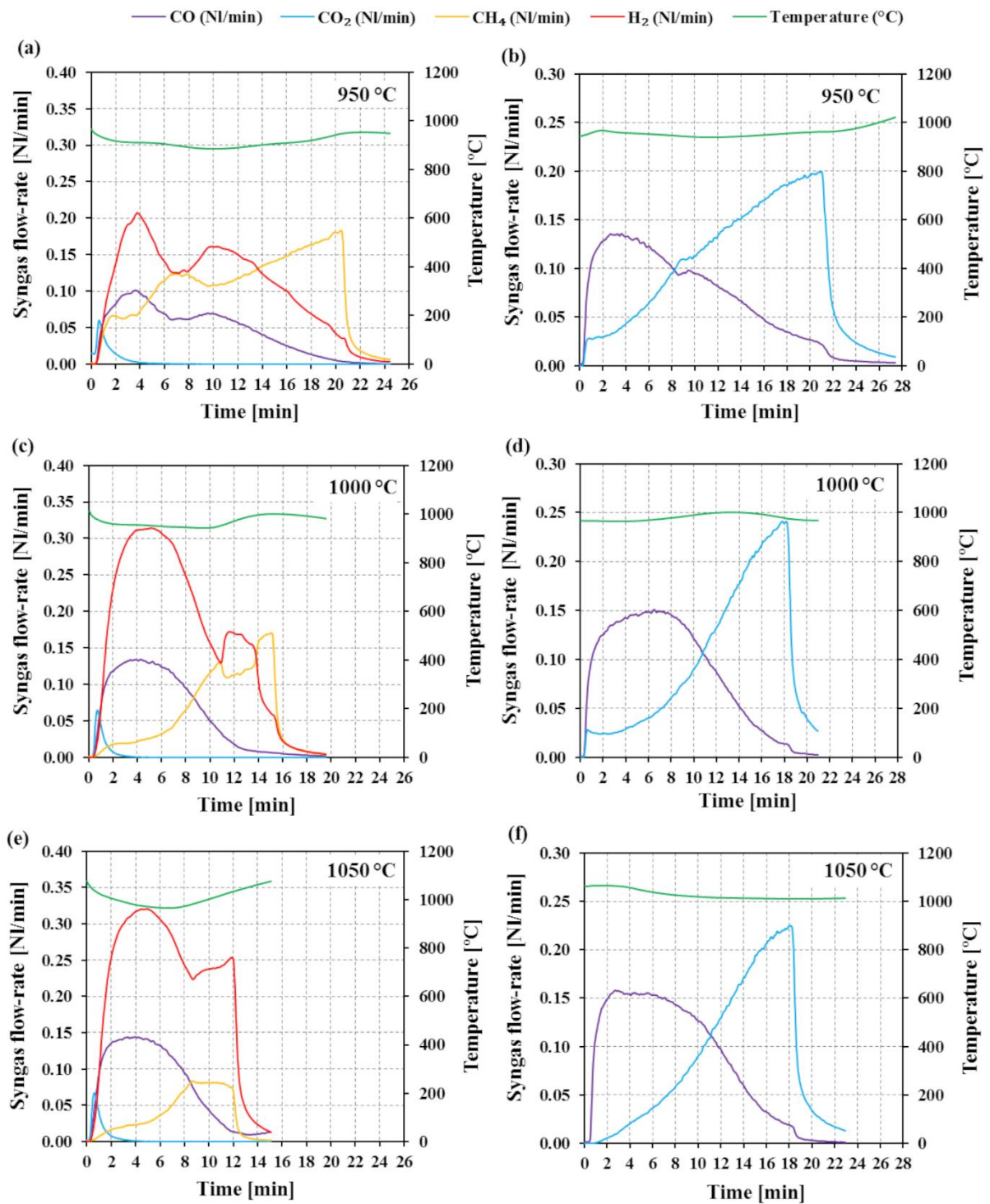


Fig.14. Evolution of the production rates of H<sub>2</sub>, CO, CO<sub>2</sub>, and CH<sub>4</sub> in the syngas along with nominal reactor temperature for reduction with CH<sub>4</sub> (a, c, and e) and oxidation with CO<sub>2</sub> (b, d, and f) of CeO<sub>2</sub>-Al<sub>2</sub>O<sub>3</sub> blend cycled isothermally at 950, 1000, and 1050 °C.

Fig. 15 shows the syngas yields quantified from the integration of the measured syngas production rates (Fig.14) during reduction and oxidation steps. As expected, the CO (CeO<sub>2</sub>+CH<sub>4</sub>), H<sub>2</sub> (CeO<sub>2</sub>+CH<sub>4</sub>), H<sub>2</sub> (CH<sub>4</sub> cracking) yields, and  $\delta_{red}$  increased with temperature, while the CO<sub>2</sub> (CeO<sub>2</sub>+CH<sub>4</sub>) yield remained the same (Fig.15a). During oxidation step (Fig.15b), an increase in the CO yield (2.89-3.12 mmol/g<sub>CeO<sub>2</sub></sub>) was observed when increasing the temperature in the range of 950-1050 °C, thereby enhancing the  $\delta_{ox}$  (0.37-0.40). The  $\delta_{ox}$  values were similar to  $\delta_{red}$ , thus confirming complete ceria re-oxidation with CO<sub>2</sub>

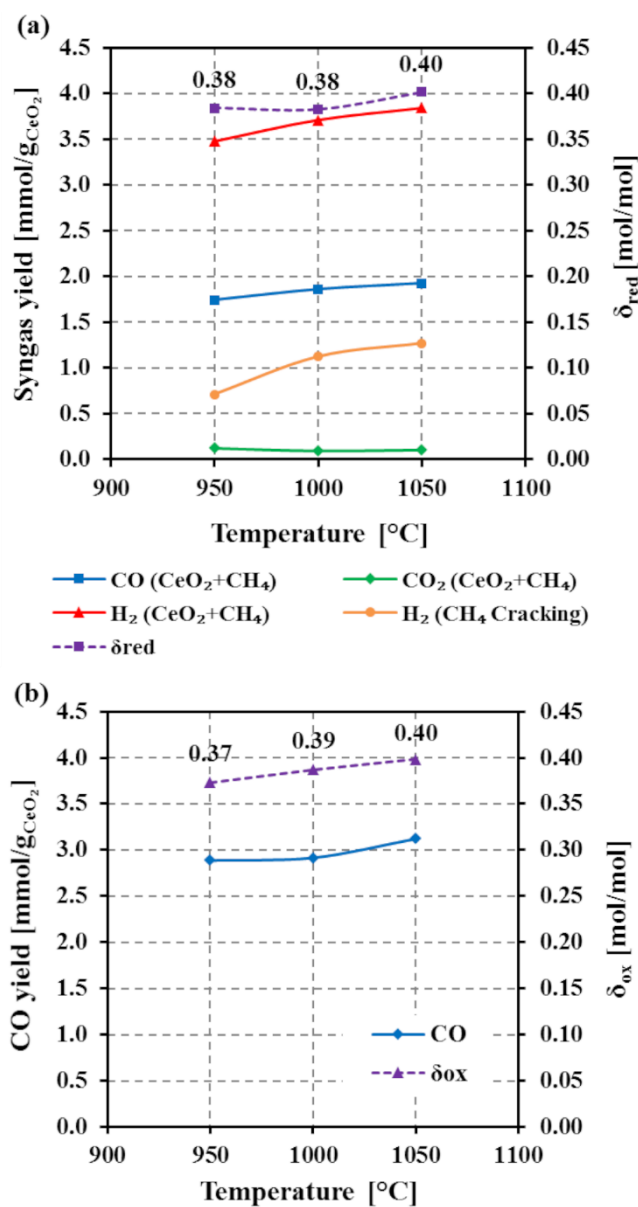


Fig. 15. Effect of temperature on syngas yields,  $\delta_{\text{red}}$ , and  $\delta_{\text{ox}}$  for (a) reduction with  $\text{CH}_4$  and (b) oxidation with  $\text{CO}_2$  of  $\text{CeO}_2\text{-Al}_2\text{O}_3$  blend cycled isothermally ( $\text{CH}_4$  flow-rate of 0.2 Nl/min).

A temperature increase significantly enhanced the reactor performance (Fig.16a), especially methane conversion (37.2-75.8%). Fig.16b compares the total syngas yield obtained from ceria cycles (sum of both steps) to the theoretical maximum yield (assuming that  $\delta_{\text{max}}=0.5$  in Eqs. (1) and (3), thereby yielding both 1 mol CO and 1 mole  $\text{H}_2$  per mole  $\text{CeO}_2$ ). Increasing temperature promoted the overall  $\text{H}_2$  and CO yields with maximum measured values of 5.11 and 5.04 mmol/ $\text{g}_{\text{CeO}_2}$  at 1050 °C, respectively, while the maximum theoretical  $\text{H}_2$  and CO yields that can be expected with  $\text{CO}_2$  are 5.81 mmol/ $\text{g}_{\text{CeO}_2}$ . Note that the amounts of both  $\text{H}_2$  and CO produced by side reactions ( $\text{CH}_4$  cracking:  $\text{CH}_4 \rightarrow \text{C} + 2\text{H}_2$  and carbon gasification:  $\text{C} + \text{CO}_2 \rightarrow 2\text{CO}$ ) in both steps were taken into account in Fig.16b. The CO yield was close to the  $\text{H}_2$  yield throughout the range. In addition, U was in the range 1.11-1.19 (versus 1.31 for a stoichiometric reaction with  $\delta_{\text{max}}=0.5$ ).

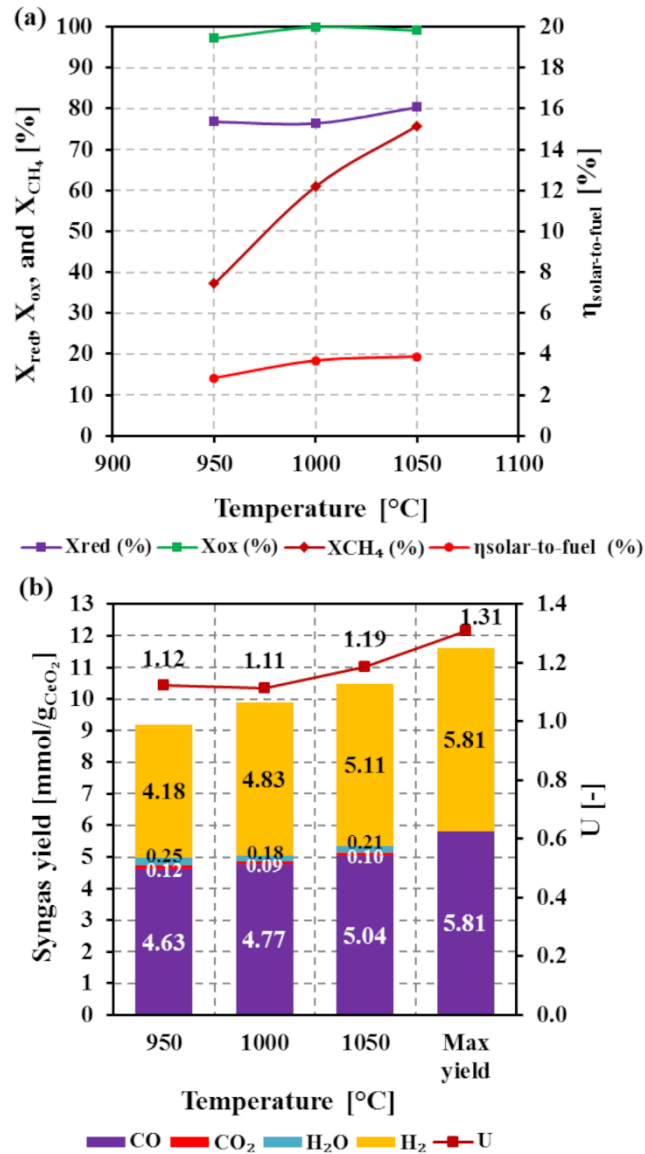


Fig. 16. Effect of temperature on (a) ceria reduction yield, methane conversion, and solar-to-fuel energy conversion efficiency, and (b) energy upgrade factor and total syngas yields obtained from both reduction and oxidation steps.

### 3.5 Assessment of thermochemical stability during cycling

A pristine ceria reticulated foam (17.0152 g) sintered at 1000 °C for 6 hr was used (Fig.17a) to experimentally investigate the cycling stability during 6 consecutive cycles at 1000°C (CH<sub>4</sub> flow rate of 0.2 Nl/min for reduction step and H<sub>2</sub>O flow-rate of 200 mg/min for oxidation step). N<sub>2</sub> was used as a carrier gas (2.2 Nl/min).

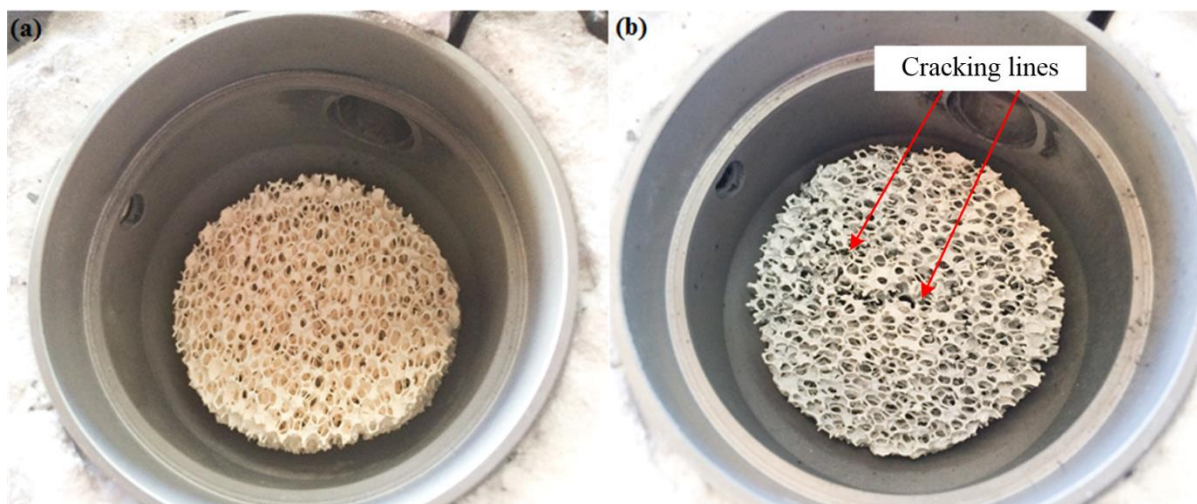


Fig. 17. Ceria reticulated foam (ST-1000) (a) before the cycling stability test and (b) after six consecutive cycles at 1000 °C.

Fig. 18 shows the syngas yields and reaction extents over six consecutive cycles during ceria reduction with methane (Fig.18a) and ceria oxidation with H<sub>2</sub>O (Fig.18b). As expected, the H<sub>2</sub> (CeO<sub>2</sub>+CH<sub>4</sub>), CO, and CO<sub>2</sub> yields were constant over the whole cycling (ranging between 3.39-3.68 mmol/g<sub>CeO<sub>2</sub></sub> for H<sub>2</sub>, 1.69-1.84 mmol/g<sub>CeO<sub>2</sub></sub> for CO, and 0.05-0.07 mmol/g<sub>CeO<sub>2</sub></sub> for CO<sub>2</sub>, Fig.18a), thus validating ceria cycling stability. However, both small sintering and cracking lines within the sample were observed after the last cycle (Fig.17b), presumably due to its weakened structure associated with low sintering temperature (1000 °C). Nevertheless, the redox cycling performance of ceria was not altered as reflected by a minimal fluctuation of reduction extent ( $\delta_{\text{red}}$  in the range of 0.32-0.36). The H<sub>2</sub> (CH<sub>4</sub> cracking) yield fluctuated slightly (0.64-1.16 mmol/g<sub>CeO<sub>2</sub></sub>), except for cycle 1 (2.00 mmol/g<sub>CeO<sub>2</sub></sub>) in which the H<sub>2</sub> yield and  $\delta_{\text{red}}$  were much higher due to a higher reduction temperature (1050 °C) than the other cycles (the CO and CO<sub>2</sub> formed in the oxidation step were thus also higher, Fig.18b).

Likewise, the H<sub>2</sub> (CeO<sub>2- $\delta$</sub> +H<sub>2</sub>O) yield produced by Eq. (2) (Fig.18b) was fairly stable (1.94-2.05 mmol/g<sub>CeO<sub>2</sub></sub>) thus leading to a similar stable  $\delta_{\text{ox}}$  pattern (0.33-0.35). In addition, the



quantities of  $H_2(C+2H_2O)$ ,  $H_2(C+H_2O)$ ,  $CO(C+H_2O)$ , and  $CO_2(C+2H_2O)$  remained similar except for cycle 1 as mentioned above. Stable patterns in  $X_{red}$ ,  $X_{ox}$ ,  $X_{CH_4}$ ,  $\eta_{solar-to-fuel}$  and total syngas yield were consistently noticed (Fig.S7). Thus, the cycling stability of ceria can fairly be validated.

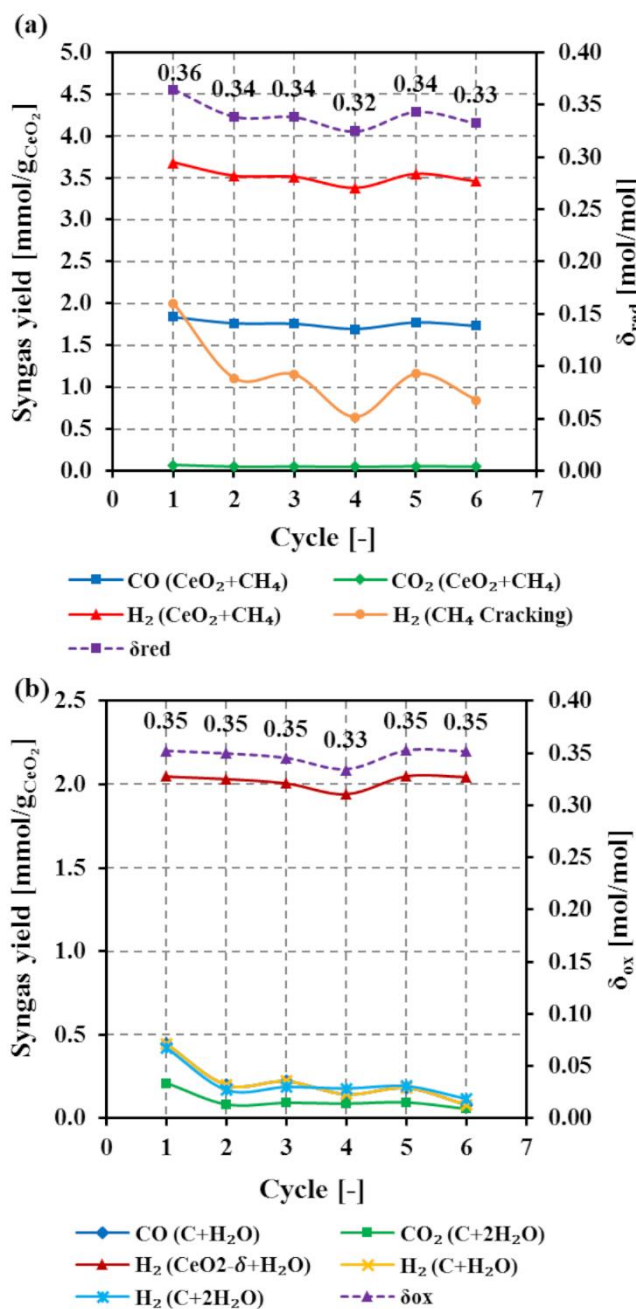


Fig. 18. Syngas yield and  $\delta$  for both (a) reduction and (b) re-oxidation of ceria during 6 consecutive redox cycles performed at 1000 °C.



#### 4. Conclusion

A solar process for methane reforming using solid oxidants has been developed, with final aim of producing syngas according to the following reaction:  $\text{CH}_4 + \text{M}_x\text{O}_y \rightarrow \text{M}_x\text{O}_{y-1} + \text{CO} + 2\text{H}_2$ . The key advantages of such a process with respect to the conventional process are: (i) generation of a gaseous mixture suitable for methanol synthesis, (ii) utilization of a solid oxidant instead of gaseous oxygen or steam water, (iii) absence of costly catalysts, and (iv) possible production of  $\text{H}_2$  (or  $\text{CO}$ )-rich gas in a second step enabling the regeneration of the starting oxide. This chemical looping reforming process has been fully demonstrated using  $\text{CeO}_2$  as the oxygen carrier material in the form of powders and reticulated porous foams within both fixed bed and volumetric solar reactor. Indeed, a directly irradiated  $1.5 \text{ kW}_{\text{th}}$  solar reactor has been successfully operated for solar-driven chemical looping methane reforming and isothermal  $\text{H}_2\text{O}/\text{CO}_2$  splitting using different ceria structures as oxygen carriers, demonstrating the reliability and flexibility of the combined process towards syngas production. A parametric study was carried out focusing on the influence of sintering temperature of the foam structure,  $\text{CH}_4$  flow-rate, operating temperature, type of oxidant ( $\text{H}_2\text{O}$  or  $\text{CO}_2$ ) and ceria structures on averaged oxygen non-stoichiometry ( $\delta$ ),  $\text{CH}_4$  conversion, syngas production, reactor performance, and thermochemical cycling stability.

- A high sintering temperature ( $1400 \text{ }^\circ\text{C}$ ) adversely affects the syngas yield, methane conversion, and reactor performance, because of both lowered solid/gas interface area and lattice oxygen mobility, thus decreasing oxygen exchange capacity.

- Increasing the  $\text{CH}_4$  flow-rate enhances  $\delta$  (maximum value up to 0.41 for ceria powder), syngas production rate, and syngas yield. However, a remarkable decrease in  $\text{CH}_4$  conversion is concomitantly observed (minimum value as low as 43% for  $\text{CeO}_2$  powder).

High CH<sub>4</sub> flow rate also favors CH<sub>4</sub> cracking reaction and carbon deposition, since the rate of methane decomposition exceeds the rate of ceria reduction. Such carbon deposition is not detrimental for the whole process since carbon is gasified in the oxidation step.

- Increasing the temperature (between 900-1050 °C) accelerates the rate of ceria reduction, which in turn significantly enhances the methane conversion (up to 77.4% for CeO<sub>2</sub>-Al<sub>2</sub>O<sub>3</sub> blend) and syngas yield and decreases the reduction step duration. However, it comes at the expense of favoring methane cracking, especially at 1050 °C. The  $\eta_{\text{solar-to-fuel}}$  is increased with both CH<sub>4</sub> flow-rate and temperature (values in the range 1.14-5.60%), while the energy upgrade factor up to 1.19 is accomplished with CO<sub>2</sub> as oxidant.

- The shape of ceria materials (packed-bed powder, foam) does not show any significant impact on both the syngas yield and  $\delta$  but rather on CH<sub>4</sub> conversion and efficiency. The ceria foam shows better performance in terms of volumetric solar radiation absorption and uniform heating with lower solar power consumption compared to the other structures, thereby upgrading  $\eta_{\text{solar-to-fuel}}$  (maximum value up to 5.6%). This implies that the foam structure is the most suitable to achieve high specific syngas production with reduced solar energy input.

- The ceria re-oxidation step is always complete ( $\delta_{\text{ox}}$  and  $\delta_{\text{red}}$  are similar), which means it is not kinetically limited, and it depends only on the extent of ceria reduction achieved during the previous reduction step. Ceria reduction ( $\delta_{\text{red}}$ ) is strongly dependent on temperature or methane flow rate, which thus denotes kinetically-controlled reaction rate.

- Stable patterns in the reduction/oxidation extents, syngas yields and  $\eta_{\text{solar-to-fuel}}$  during consecutive cycles for the ceria reticulated foam validate excellent thermal cycling stability.

The solar reactor concept is expected to be flexible in processing different ceria structures with varying particle sizes or geometries. Further work should be performed

regarding reactor upscaling and ceria porous foam structure tailoring to improve the global efficiency of the integrated isothermal solar process combining chemical looping reforming and H<sub>2</sub>O/CO<sub>2</sub> splitting.

### **Acknowledgement**

The King Mongkut's Institute of Technology Ladkrabang (KMITL), Thailand and the Franco-Thai scholarship program are gratefully acknowledged for fellowship granting.

### **References**

- [1] A. Klerk, Fischer–Tropsch Process. Kirk-Othmer Encycl Chem Technol (2013). doi:10.1002/0471238961.fiscdekl.a01.
- [2] C. Graves, S.D. Ebbesen, M. Mogensen, K.S. Lackner, Renew Sustain Energy Rev 15 (2011) 1–23. doi:10.1016/J.RSER.2010.07.014.
- [3] Q. Zheng, C. Janke, R. Farrauto, Appl Catal B Environ 160–161 (2014) 525–533. doi:https://doi.org/10.1016/j.apcatb.2014.05.044.
- [4] Q. Song, R. Xiao, Y. Li, L. Shen, Ind Eng Chem Res 47 (2008) 4349–4357. doi:10.1021/ie800117a.
- [5] G. Zhang, Y. Dong, M. Feng, Y. Zhang, W. Zhao, H. Cao, Chem Eng J 156 (2010) 519–523. doi:10.1016/j.cej.2009.04.005.
- [6] G. Zhang, A. Su, Y. Du, J. Qu, Y. Xu, J Colloid Interface Sci 433 (2014) 149–155. doi:10.1016/j.jcis.2014.06.038.
- [7] G. Zhang, Y. Du, Y. Xu, Y. Zhang, J Ind Eng Chem 20 (2014) 1677–1683. doi:10.1016/j.jiec.2013.08.016.
- [8] K. Otsuka, Y. Wang, M. Nakamura, Appl Catal A Gen 183 (1999) 317–324. doi:10.1016/S0926-860X(99)00070-8.
- [9] K. Otsuka, T. Ushiyama, I. Yamanaka, Chem Lett 22 (1993) 1517–20.

- doi:10.1246/cl.1993.1517.
- [10] K. Otsuka, Y. Wang, E. Sunada, I. Yamanaka, *J Catal* 175 (1998) 152–60.  
doi:10.1006/jcat.1998.1985.
- [11] C. Wieckert, A. Steinfeld, *J Sol Energy Eng* 124 (2001) 55–62.
- [12] T. Kodama, T. Shimizu, A. Aoki, Y. Kitayama, *Energy & Fuels* 11 (1997) 1257–1263.  
doi:10.1021/ef9700691.
- [13] H.I. Villafan-Vidales, S. Abanades, M. Montiel-Gonzalez, H. Romero-Paredes, *Energy Technol* 5 (2016) 692–702. doi:10.1002/ente.201600455.
- [14] M. Welte, K. Warren, J.R. Scheffe, A. Steinfeld, *Ind Eng Chem Res* 56 (2017) 10300–10308. doi:10.1021/acs.iecr.7b02738.
- [15] P. Furler, J. Scheffe, D. Marxer, M. Gorbar, A. Bonk, U. Vogt, *Phys Chem Chem Phys* 16 (2014) 10503–10511. doi:10.1039/C4CP01172D.
- [16] D. Marxer, P. Furler, M. Takacs, A. Steinfeld, *Energy Environ Sci* 10 (2017) 1142–1149. doi:10.1039/C6EE03776C.
- [17] S. Abanades, P. Charvin, G. Flamant, P. Neveu, *Energy* 31 (2006) 2805–2822.  
doi:10.1016/j.energy.2005.11.002.
- [18] K. Otsuka, M. Hatano, A. Morikawa, *J Catal* 79 (1983) 493–496. doi:10.1016/0021-9517(83)90346-9.
- [19] K. Li, H. Wang, Y. Wei, D. Yan, *Appl Catal B Environ* 97 (2010) 361–372.  
doi:10.1016/j.apcatb.2010.04.018.
- [20] K. Li, H. Wang, Y. Wei, D. Yan, *Chem Eng J* 156 (2010) 512–518.  
doi:10.1016/j.cej.2009.04.038.
- [21] T. Shimizu, Y. Kitayama, T. Kodama, *Energy & Fuels* 15 (2001) 463–469.  
doi:10.1021/ef000200w.
- [22] A. Steinfeld, A. Frei, P. Kuhn, D. Wuillemin, *Int J Hydrogen Energy* 20 (1995) 793–

804. doi:10.1016/0360-3199(95)00016-7.
- [23] M.M. Nair, S. Abanades, *Energy & Fuels* 30 (2016) 6050–6058.  
doi:10.1021/acs.energyfuels.6b01063.
- [24] O.T. Sørensen, *J Solid State Chem* 18 (1976) 217–233. doi:10.1016/0022-4596(76)90099-2.
- [25] P.T. Krenzke, J.H. Davidson, *Energy & Fuels* 28 (2014) 4088–4095.  
doi:10.1021/ef500610n.
- [26] S. Chuayboon, S. Abanades, S. Rodat, *Chem Eng J* 356 (2019) 756–770.  
doi:10.1016/j.cej.2018.09.072.
- [27] P. Furler, J. Scheffe, M. Gorbar, L. Moes, U. Vogt, A. Steinfeld, *Energy & Fuels* 26 (2012) 7051–7059. doi:10.1021/ef3013757.
- [28] N. Siegel, R. Diver, J.E. Miller, T. Garino, S. Livers, ASME. *Energy Sustainability, ASME 2009 3rd International Conference on Energy Sustainability*, 2 (2009) 431-437.  
doi:10.1115/ES2009-90093.
- [29] F.A. Costa Oliveira, M.A. Barreiros, S. Abanades, A.P.F. Caetano, R.M. Novais, R.C. Pullar, *J CO<sub>2</sub> Util* 26 (2018) 552–563. doi:10.1016/j.jcou.2018.06.015.
- [30] D. Arifin, A.W. Weimer, *Sol Energy* 160 (2018) 178–85.  
doi:10.1016/j.solener.2017.11.075.
- [31] M. Roeb, C. Sattler, R. Klüser, N. Monnerie, L. de Oliveira, A.G. Konstandopoulos, *J Sol Energy Eng* 128 (2005) 125–133.
- [32] T. Kodama, N. Gokon, *Am Chem Soc* (2007) 4048–4077. doi:10.1021/cr050188a.
- [33] P. Furler, J.R. Scheffe, A. Steinfeld, *Energy Environ Sci* 5 (2012) 6098–103.
- [34] L.J. Venstrom, N. Petkovich, S. Rudisill, A. Stein, J.H. Davidson, *J Sol Energy Eng* 134 (2011) 11005–11008.
- [35] T. Kodama, S. Bellan, N. Gokon, H. Seok Cho, *Solar Energy* 156 (2017) 113-132.

- [36] E. Alonso, M. Romero, *Renew Sustain Energy Rev* 41 (2015) 53–67.
- [37] H.I. Villafán-Vidales, C.A. Arancibia-Bulnes, D. Riveros-Rosas, H. Romero-Paredes, C.A. Estrada, *Renew Sustain Energy Rev* 75 (2017) 894–908.
- [38] E. Koepf, I. Alxneit, C. Wieckert, A. Meier, *Applied Energy* 188 (2017) 620-651.
- [39] C. Agrafiotis, M. Roeb, C. Sattler, *Renewable and Sustainable Energy Reviews* 42 (2015) 254–285.
- [40] N. Piatkowski, C. Wieckert, A.W. Weimer, A. Steinfeld, *Energy & Environmental Science* 4 (2011) 73-82.
- [41] M. Puig-Arnavat, J.C. Tora, E.A Bruno, A. Coronas, *Solar Energy* 97 (2013) 67–84.
- [42] K. Otsuka, E. Sunada, T. Ushiyama, I. Yamanaka, *107* (1997) 531–536.  
doi:10.1016/S0167-2991(97)80386-2.